CHAPTER 17

Five Coordination

17.1 INTRODUCTION

Throughout this book, we have stressed one technique for understanding the molecular orbitals of complicated molecules, namely, their construction from the valence orbitals of smaller subunits. In the organometallic area, this is particularly useful since the molecules consist of an ML_n unit bonded to some organic ligand. For this purpose, we need to build up a library of valence orbitals for common ML_n fragments, where $n = 2$–5 and L is a generalized two-electron σ donor ligand. We could do this by interacting an ensemble of L_n functions with a transition metal, just as was carried through for the octahedron (Section 15.1) and square plane (Section 16.1) cases. However, an easier method [1–3] starts with the valence, metal-centered orbitals of the octahedron and square plane. One or more ligands are then removed. This is illustrated in Chart 17.1. The valence orbitals of a C_{4v} ML_5 fragment, **17.2**, can easily be derived by taking those of ML_6, **17.1**, and considering the perturbation induced by removing one ligand. A C_{2v} ML_4 species, **17.3**, is derived by removing two cis ligands from ML_6, and removal of three *fac* ligands will yield the C_{3v} ML_3 fragment, **17.4**. We shall be primarily concerned with the geometry perturbation on going from **17.1** to **17.2** in this chapter. Now, those fragments, **17.2**-**17.3**, can be distorted to give fragments of other types. For example, the C_{2v} ML_4 fragment can easily be distorted to a C_{4v} structure, **17.5**, or a tetrahedron. Likewise, we find it useful to generate the levels of **17.6** from those of the square pyramid.

Once the orbitals of a trigonal bipyramid have been derived, they can be used in turn to establish the orbitals of a C_{3v} ML_4 fragment like **17.7** which may then be distorted to a tetrahedron, and so on. Thus, the reductive approach illustrated in Chart 17.1 offers many ways to interrelate the orbitals of different systems. The fragments are interesting molecules in their own right, and we shall spend some time with their structure and dynamics. Our other starting point is the square plane, **17.8**.

Orbital Interactions in Chemistry, Second Edition.
Thomas A. Albright, Jeremy K. Burdett, and Myung-Hwan Whangbo.

CHART 17.1

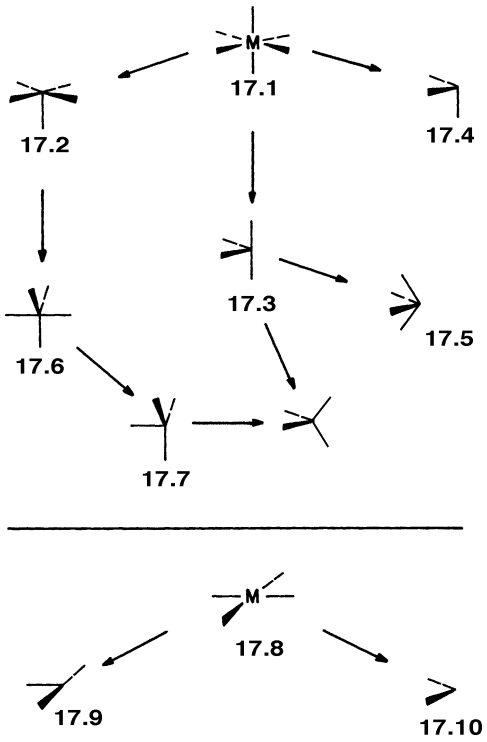

Removal of one ligand gives a C_{2v} ML_3 fragment, **17.9**. We shall see in Section 18.1 that the orbital structure of **17.9** is very similar to that of the C_{4v} ML_5 fragment, **17.2**. Removing two cis ligands from **17.8** gives **17.10**, with orbitals similar to those of **17.3**. This correspondence between different ML_n fragments is an important way to simplify and unify organometallic chemistry and forms a common thread running through Chapters 18–20.

17.2 THE C_{4V} ML_5 FRAGMENT

On the left of Figure 17.1 are listed the metal-centered *d* blocks of orbitals for octahedral ML_6. In Section 15.1 (see Figure 15.1), we established that there is a lower group of three levels, *xz*, *yz*, and *xy*, using the coordinate system at the top of Figure 17.1, which have t_{2g} symmetry. These are filled for a saturated (18 electron) d^6 complex. At much higher energy is the $2e_g$ set. It will be empty in most organometallic examples and consists of $x^2 - y^2$ and z^2 antibonding to the ligand lone pairs. When one ligand is removed from the octahedron [1], to a first approximation, the t_{2g} set is left unaltered. The resultant levels are labeled as $e + b_2$ in the C_{4v} point group of the fragment. No hybridization or energy change is introduced because the lone pair of the missing ligand is orthogonal to t_{2g}. The same is true for the $x^2 - y^2$ component of $2e_g$. Suppose that the ligand removed from $Cr(CO)_6$ was CO—a π acceptor [4]. Then, the *xz* and *yz* components of t_{2g} would rise slightly in energy and *xy* is left untouched. Consequently, a relatively small energy gap will be introduced between *e* and b_2. The major perturbation occurs with the z^2 component of $2e_g$. That orbital, labeled a_1, will be greatly stabilized. Removing the ligand loses one strong antibonding interaction between metal z^2 and the ligand. The a_1 level also becomes hybridized by mixing some *s*

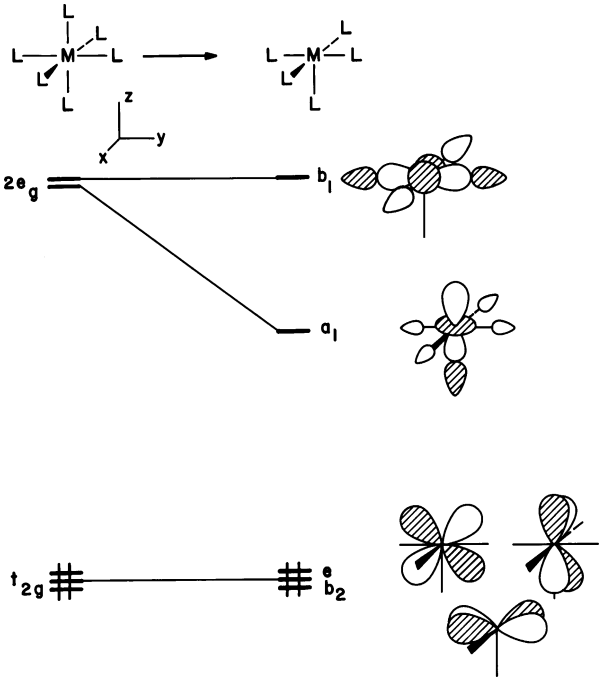

FIGURE 17.1
Orbital correlation diagram for the octahedron to square pyramid conversion. Only the *d* orbital part of the diagram is shown. Note the rehybridization of z^2 toward the empty coordination site.

and *z* characters in a way that reduces the antibonding between the metal and surrounding ligands. The origin of this hybridization in a_1 is not much different from that in the variation of cis and trans L–M–L angles in ML_6 (Section 15.3). We shall outline one way to view the resultant hybridization. The O_h ML_6 to C_{4v} ML_5 conversion involves a reduction of symmetry. The $2a_{1g}$ orbital (see Figure 15.1) and the *z* component of $2t_{1u}$ lie close in energy to $2e_g$. Both orbitals also will have a_1 symmetry upon loss of the CO ligand. Consequently, they mix into the z^2 component of $2e_g$, **17.11** (in first order), in a way that reduces the antibonding between the metal and its surrounding ligands. Recall that $2a_{1g}$ and $2t_{1u}$ lie at higher energy than $2e_g$; thus, they mix

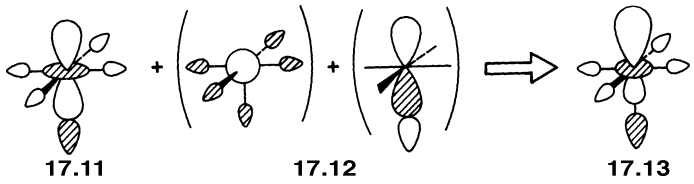

17.11 **17.12** **17.13**

into **17.11** in a bonding manner. This is diagrammed in **17.12**. Notice that it is the phase relationship shown for the metal *s* and *z* in **17.12** to the ligand lone pairs in **17.11** that sets the mixing sign. $2a_{1g}$ and $2t_{1u}$ are, after all, concentrated at the metal. Therefore, the largest interorbital overlap will occur between the atomic components of **17.12** at the metal and the lone pairs in **17.11**. The resultant orbital, **17.13**, is stabilized further by this mixing process, and it becomes hybridized out away from the remaining ligands, toward the missing one. The a_1 orbital is empty for a d^6 fragment. It obviously will play a crucial role when real molecules are constructed from the ML_5 fragment. Its directionality and the fact that it lies at moderate energy make it a superlative σ-accepting orbital. An MO plot at the extended Hückel level of this orbital in $Cr(CO)_5$ is shown at the top of Figure 17.2. Notice the distinct hybridization out toward the missing carbonyl. Returning to Figure 17.1,

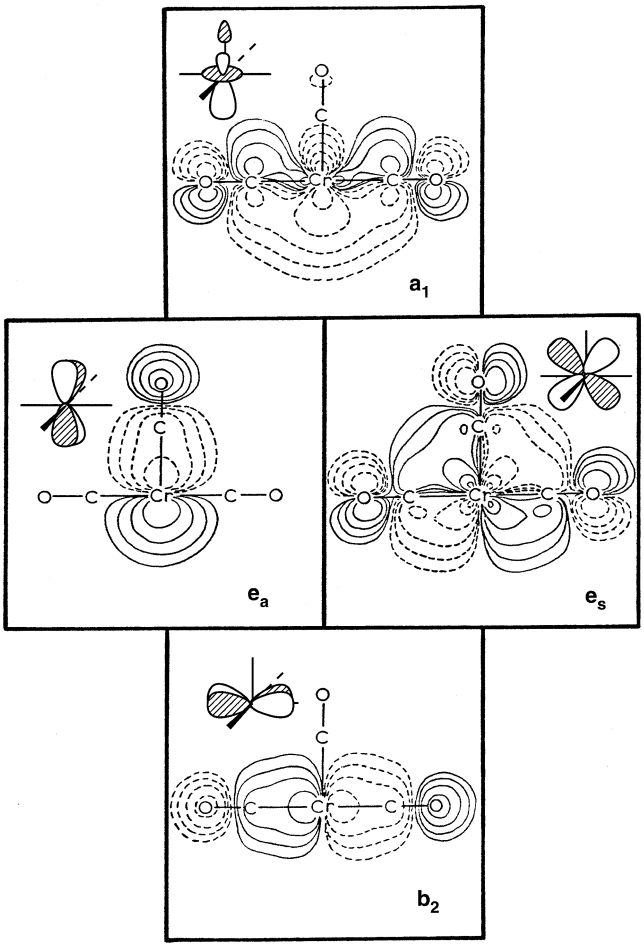

FIGURE 17.2

Contour plots at the extended Hückel level of the five important valence orbitals in $Cr(CO)_5$. The plots for e_a and b_2 are 0.5 Å from the Cr atom and parallel to the *yz* plane (see Figure 17.1).

below a_1 lies a nest of three "t_{2g} like" orbitals that are utilized for π bonding, *xz*, *yz* (*e* symmetry), and *xy* (b_2). Plots of these three MOs for $Cr(CO)_5$ are also shown in Figure 17.2. The antisymmetric component of the *e* set, e_a, and the b_2 orbital are plotted in a plane parallel to the *yz* plane at a distance of 0.5 Å from the Cr atom. It is very clear that these three MOs have large amounts of CO π^* character mixed into them. How much π^* mixes into these levels is certainly a question of methodology and parameterization (basis set choices, etc.). Looking back to the plots in Chapters 15 and 16 using DFT and HF methods would suggest somewhat less involvement of CO π^*. But, rather than being concerned with exact quantitative matters, we shall take a more qualitative, global view. Before we use the ML_5 unit as a building block for larger molecules, it is instructive to examine it as a molecule in its own right.

17.3 FIVE COORDINATION

We have looked at the orbital properties of the main group AH_5 molecules in Chapter 11. Two basic structures are known, the square pyramid (**17.14**) and the trigonal bipyramid (**17.15**). The ideal square pyramid has C_{4v} symmetry. As a result,

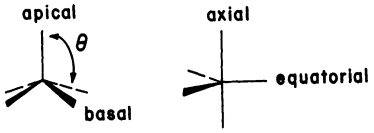

17.14 17.15

there are two different ligand sites, apical and basal, and there is one angular degree of freedom, θ. The ideal trigonal bipyramid has D_{3h} symmetry, so there are again two different ligand sites, equatorial and axial. A whole spectrum of geometries between the two extremes is also found in practice. The interconversion of the two geometries can occur via the Berry pseudorotation process that shall be examined shortly.

The energy levels of the square pyramid [5] with $\theta = 90°$ have been derived in Section 17.1. First, we see how they change in energy as the angle θ varies. This is done in the Walsh diagram for FeH_5^+ at the extended Hückel level in Figure 17.3. Notice that this model is free from any π effects. As θ increases from 90°, the σ overlap of the basal ligands with z^2 and $x^2 - y^2$ decreases (Figure 17.3); they become less antibonding and lowered in energy. In other words, the first-order correction to the energy in both cases is negative using geometric perturbation theory. A plot of the z^2 MO at the B3LYP DFT level for FeH_5^+ is also shown on the upper right side of the figure. Concurrently, σ interaction with the *xz*, *yz* pair of orbitals is turned on, so these levels are pushed to higher energy. Such a geometry change also changes the shape of these metal *d*-based orbitals since they become hybridized with the $(n+1)p$ metal orbitals. This is shown for the pair of *e* MOs on the right side of Figure 17.3. A plot of the *yz* component of the *e* set for FeH_5^+ is shown in the middle right side of the figure. We have seen this *d*–*p* mixing previously in Section 15.4 for a related angular geometry change. The resulting hybridization out away from the ligands is entirely analogous to this previous case. From a geometrical perturbation theory perspective, there is no change in the energy to first order since at $\theta = 0°$, the *e* set is

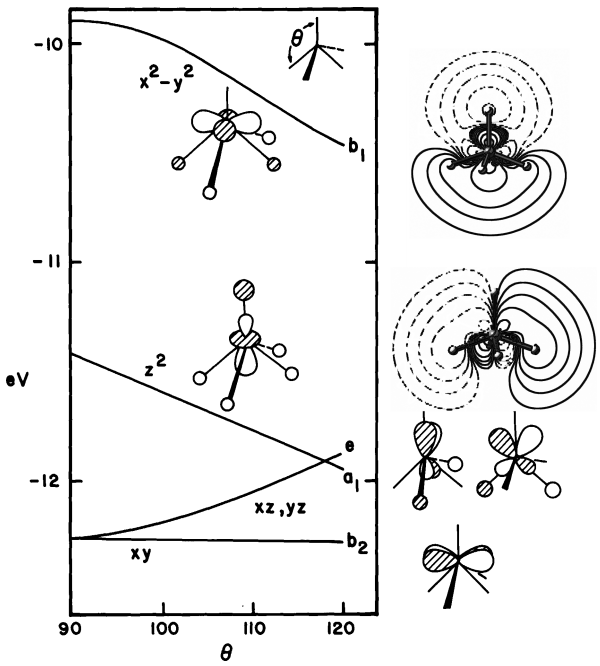

FIGURE 17.3
Orbital correlation diagram for the metal *d* orbitals on bending a square pyramid.

TABLE 17.1 Some Apical–M–Basal Bond Angles, θ, in Square Pyramidal Molecules as a Function of Electronic Configuration

Compound	d^n	θ (degrees)	CCDC Entry[a]
$Nb(OR)_2Cl_3$	d^0	102.7	ZEQTEU
$Ta(NR_2)_5$	d^0	104.2	AKINAJ
Ti(OMe)(porp)[b]	d^2	107.2	BULXIP
$Mo(SR)_5^-$	d^2	107.8	DIZMEE
$Re(CO)_3(PR_3)_2^+$	d^6	93.3	PIWWEX
Ir(porp)(CH_2-*p*-tol)	d^6	92.1	VOFDAW
$Ru(PPh_3)_3(CO)_2$	d^8	105.1	POWCUZ
$Ni(CN)_5^{3-}$	d^8	100.2	EDCRCN
$Zn(NR_3)_4Cl^+$	d^{10}	104.2	MENLAS
Cd(porp)(pyr)	d^{10}	107.4	JITDOG
Fe(porp)(imid)[c]	hs d^6	101.7	KIMGAO
Fe(porp)(imid)CO	ls d^6	89.1	FATWUS

[a]Cambridge Crystallographic Data Center entry.
[b]porp = porphyrin.
[c]imid = imidazole.

purely *xz* and *yz*. However, when the metal *x* and *z* are introduced into this *e* set, they bring in the ligand *s* AOs in a bonding manner, and the latter make antibonding with the *e* set hence destabilizing it. Notice that the ligand-based *e* set will then be stabilized upon increasing θ. Finally, the b_2 orbital stays at a constant energy and remains nonbonding with respect to the ligand σ donors.

Since the *d* orbital energies of the ML_5 square pyramid change significantly with the angle θ, the details of the geometry of such species will depend upon the number of *d* electrons and how the orbitals are occupied. Table 17.1 is a collection of some representative square pyramidal molecules where θ is the averaged apical-metal-basal bond angle. The d^0–d^2 molecules are expected to have $\theta > 90^\circ$ since, as just mentioned, the ligand-based *e* set is stabilized upon bending. The first four entries in Table 17.1 illustrate this with $\theta = 102.7^\circ$–107.8°. There are three d^0 $Ta(CH_2R)_5$ molecules that have been structurally determined: $\theta = 111.1^\circ$ for R = H [6], $\theta = 110.7^\circ$ for R = Ph [7], and $\theta = 111.0^\circ$ for R = *p*-tol [8]. Furthermore, $\theta = 113.6^\circ$ for the d^1 $Mo(CH_3)_5$ [6]. Low spin d^6 species are expected to be close to a flat pyramid ($\theta = 90^\circ$) since *xz* and *yz* (filled for a d^6 system) rise in energy as θ increases. The two examples in Table 17.1 are in fact close to this estimate. We shall shortly cover the dynamics associated with d^6 $Cr(CO)_5$ in some detail. The computed gas-phase structure is one where $\theta = 92^\circ$ [9]. Low spin d^8 species where z^2 is occupied are more distorted ($\theta > 90^\circ$). This is a trend found in general, and the examples of Table 17.1 are typical of complexes with this electron count. The $x^2 - y^2$ orbital is also stabilized upon increasing θ; thus, it is tempting to argue that the larger values of θ for the two d^{10} complexes in Table 17.1 can be attributed to the occupation of $x^2 - y^2$. But, it is also true that the *d* AOs of Zn and Cd lie at very low energies, see Figure 15.2, and, therefore bonding between the *d* AOs and the ligand σ donor functions is expected to be minimal. A better example is given by high spin d^8 complexes that have the electronic configuration $(xy)^2(xz/yz)^4(z^2)^1(x^2 - y^2)^1$. An example of great importance is deoxyhemoglobin where the iron atom in a heme unit lies in a site of square pyramidal coordination. There are four such heme units, connected to peptide chains, in hemoglobin [10]. Commensurate with the high spin d^6 electronic configuration, θ, is larger than 90°. A model given in the second to last entry in Table 17.1 is shown in **17.16**. On the coordination of O_2, the iron atom becomes six coordinate and the spin state changes to low spin. Both of these

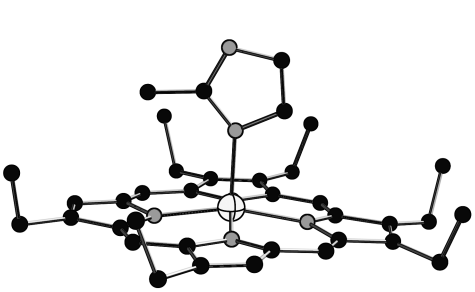

17.16

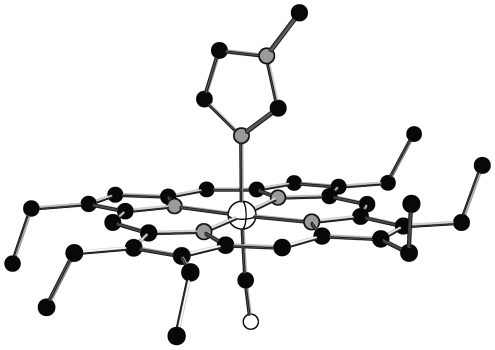

17.17

factors lead to a θ angle of about 90° in oxyhemoglobin. Thus, the stereochemical change on oxygenation leads to a considerable movement of the iron atom and, of course, the imidazole ring attached to it in the apical position of the square pyramid shown in a model where CO (rather than O_2) is used as the sixth ligand in **17.17**. Connected to the imidazole ring is the organic peptide part of the molecule. The deformations induced in this framework by the movement on going to **17.17** have been suggested to be important for the triggering of the important cooperative peptide reorganization process upon oxygen binding of one heme unit. Such movement exposes the other heme groups, so that attack by further O_2 molecules is facilitated.

Just as the electronic configuration is very important in determining the geometry along the deformation coordinate **17.14**, so too is it important in influencing the relative stabilities of the square pyramid and trigonal bipyramid along the related coordinate **17.18**. A minor complication arises in that the obvious

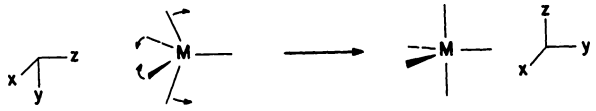

17.18 **17.19**

axis choice in the two molecules is different (**17.18** versus that in **17.19**) so that the z^2 orbital of the trigonal bipyramid becomes the $x^2 - y^2$ orbital of the square pyramid. The molecule, of course, does not know about *x*, *y*, *z* axes; these labels are there to identify orbitals. Figure 17.4 shows the Walsh diagram that correlates the orbitals for the two geometries. On the far right, the orbitals of a square pyramid are listed for a geometry with $\theta \sim 90°$. The basic motion that is followed in Figure 17.4 takes the square pyramid (**17.18**) to a trigonal bipyramid (**17.19**), by decreasing one trans L–M–L angle in the *yz* plane, ϕ, and decreasing two equatorial angles in the *xy* plane. Using the coordinate system at the upper left side of Figure 17.4, the *xz*, b_2, level for the square pyramid is unchanged along this pathway. It becomes one member of the e″ set at the trigonal bipyramidal geometry. The other member of e″ is derived from *yz*. As the one trans L–M–L angle is increased, the ligands move into the node of *yz*, causing this orbital to be stabilized. (This also results in the loss of hybridization with metal *y*.) The *xz* orbital of the square pyramid is destabilized. As the equatorial L–M–L angles in the *xy* plane are increased, the lone pair on the ligand increases its antibonding interaction with *xy*. This is reduced somewhat by increased mixing of metal *x* character. Ultimately, at the trigonal bipyramidal geometry, this orbital lies at moderate energy and is substantially hybridized out away from the ligands in the *xy* plane. A contour plot in the *xy* plane of this MO for $Fe(CO)_5$ is given in **17.20** from a

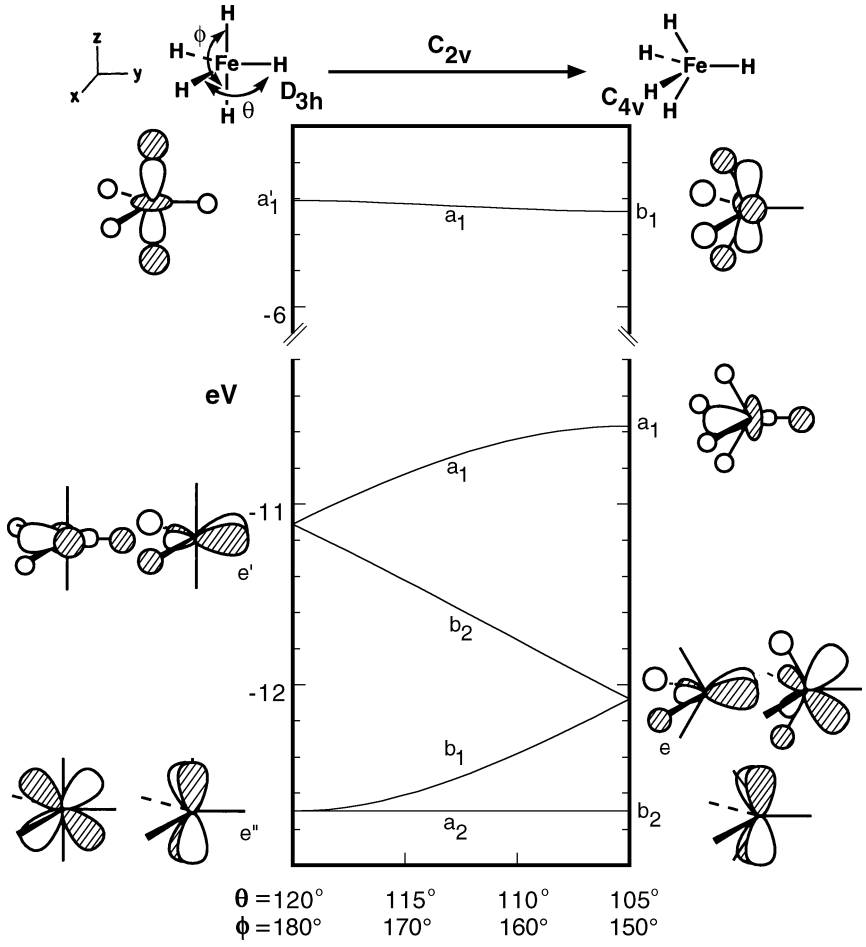

FIGURE 17.4

A Walsh diagram (at the extended Hückel level) for the metal *d* orbitals that connect square pyramidal, C_{4v}, and trigonal bipyramidal, D_{3h}, geometries.

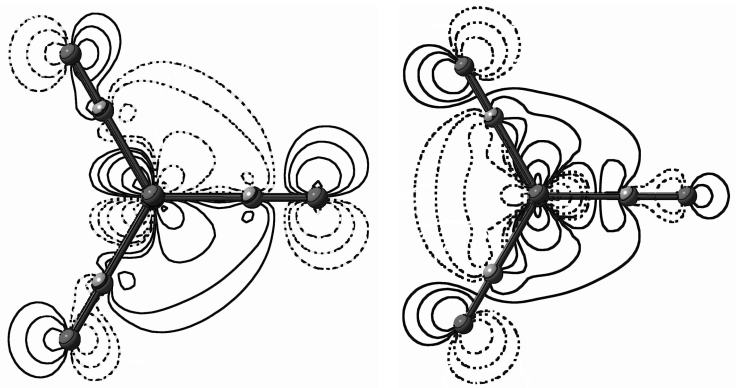

17.20 **17.21**

computation using the B3LYP hybrid functional. Along with the hybridization, note the large involvement of CO π^* particularly with the carbonyl ligand on the right side of the molecule. What happens to the two highest levels of the square pyramidal and trigonal bipyramidal geometries of Figure 17.4 is more difficult to describe. The z^2

and $x^2 - y^2$ "character" of these two levels switch. One way we can trace this intermixing is by noting that the symmetry of the molecule is C_{2v} at a geometry intermediate between the two extremes. The three orbitals that we have just examined are of $a_2 + b_1 + b_2$ symmetry. The two higher orbitals are both of a_1 symmetry. They can, and will, intermix along the reaction path. Starting from the square pyramidal side, the z^2 orbital will mix some $x^2 - y^2$ character into it until, at the trigonal bipyramidal structure, it is predominantly $x^2 - y^2$. (Remember that we have changed the coordinate system. It would become an $x^2 - z^2$ orbital if we had stayed with the axis system in **17.18**.) Two ligands in the *xy* plane move into the nodal plane of this $x^2 - y^2$ function. Furthermore, metal *y* mixes into the orbital in a bonding way to the three ligands in the *xy* plane. Therefore, this level is stabilized, and it becomes the other member of the e′ set at the trigonal bipyramidal geometry. A contour plot of this MO in $Fe(CO)_5$ is displayed in **17.21**. Again note the substantial π^* involvement for the two CO ligands on the left side of the molecule. The two members of the e′ set in the trigonal bipyramid are ideally hybridized and lie at moderately high energies, so they make excellent interactions with π acceptor orbitals that lie in the *xy* plane. We shall see several ramifications of this fact later on. The highest *d*-based orbital at the square pyramid that one would normally call $x^2 - y^2$ mixes some z^2 character into itself. At the trigonal bipyramidal geometry, it is primarily z^2, antibonding to the surrounding ligands. There is some metal *s* character in this orbital that reduces the antibonding interactions with the ligands in the *xy* plane.

The level structure for the valence levels of the trigonal bipyramid is worth studying with some care. At low energy, there is an e″ orbital, a pure metal *d* combination, which is orthogonal to the ligand lone pairs. At intermediate energy are two hybridized metal functions of e′ symmetry. At higher energy, a_1 is fully metal–ligand antibonding. What has been left off this diagram are the five metal–ligand bonding orbitals (**17.22**). Except for $2a_1$ (and the z^2 orbital in Figure 17.4), these are

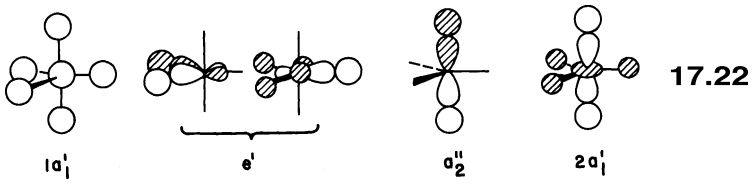

17.22

exactly analogous to the orbitals of the AH_5 main group compound (see the left side of Figure 14.17). We have introduced a strong mixing with metal *d* orbitals, so that e′ in **17.22** is a mixture of $x^2 - y^2$ and *xy* character as well as *x* and *y* at the metal. The e′ set displayed in Figure 17.3 are the nonbonding components of this three-orbital pattern. Likewise, the nonbonding $2a_1$ orbital of AH_5 will now find a perfect symmetry match with metal z^2. The $2a_1$ level in **17.22** is the bonding component, and a_1 shown at the upper left of Figure 17.4 is the antibonding partner.

We shall take a short aside here to examine the photoelectron spectrum of $Fe(CO)_5$. This is a trigonal bipyramidal molecule in the gas phase and as a crystalline solid. The formal oxidation state is Fe(0), and so, the molecule is a d^8 complex that means that it should have the electron configuration $(e'')^4(e')^4$ by the inspection of the level ordering on the left side of Figure 17.4. The photoelectron spectrum of this compound has been studied a number of times [11–14]. The 40 eV photoelectron spectrum of $Fe(CO)_5$ [11] is given in Figure 17.5. The asterisks correspond to ionizations from free CO. The peaks at 8.5 and 9.8 eV have been assigned to ionizations from the e′ and e″ MOs, respectively. The peaks from 14.1 to 16.5 eV are thought to originate from CO 1π- and 3σ-based orbitals (see Figure 6.7 for the orbitals of CO), and those from 17.9 to 20.0 eV are derived

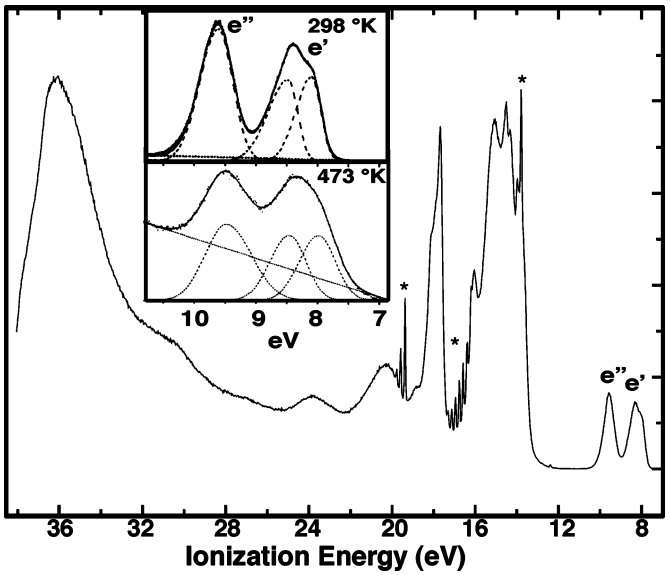

FIGURE 17.5

The 40 eV photoelectron spectrum of $Fe(CO)_5$ taken from Reference [11]. The asterisks show the positions of peaks due to free CO. The two insets at the top center of the figure are expansions of the low energy regions at two temperatures and are taken from Reference [12].

from CO 2σ [14]. What is intriguing about the PE spectrum is that the band associated with the e' set is decidedly asymmetrical. An expansion of the two lowest ionizations is shown [12] in the two insets at the top of the figure. The e' ionization can be deconvoluted into two peaks. The reason for this lies in the fact that the $^2E'$ state of $[Fe(CO)_5]^+$ ion, resulting from the ionization, is Jahn–Teller unstable (see Section 7.4.A). The symmetric direct product yields possible distortions of a_1', a_2', and e' symmetry. The normal modes for a trigonal bipyramid are shown in Appendix III. It is the e' normal mode that can split the degenerate state into two. An elegant analysis [12] of this shows that a motion like that in Figure 17.4 to C_{2v} symmetry will split the $^2E'$ state into $^2B_2$ and $^2A_1$ (a single electron occupies either b_2 or a_1 upon distortion to C_{2v}). Now, the $^2E''$ ion is also Jahn–Teller unstable and the symmetric direct product also points to the same vibrational mode of e' symmetry as creating two states of $^2B_1$ and $^2A_2$ symmetry. One can see from Figure 17.4 that the b_2–a_1 splitting is large upon deformation as opposed to that for the b_1–a_2 set and this in turn leads to a larger electronic state difference for the former. The inset in Figure 17.5 also shows that the Jahn–Teller splitting in the $^2E'$ state becomes larger as the temperature is raised. At 298 K, it is 0.38 eV and this increases to 0.47 eV at 473 K [12]. At higher temperatures, the mean vibrational distribution maximizes at larger nuclear displacements from the D_{3h} geometry and, therefore, the splitting between the two electronic states becomes larger.

From Figure 17.4, we can comment on the preferred geometries of ML_5 compounds as a function of d electron configuration. Recall that there is a slight favoring of the D_{3h} trigonal bipyramidal geometry for what would be the d^0 configuration from our discussion of main group stereochemistry in Section 14.3 in accordance with the VSEPR model. But, here there is strong d orbital involvement in the bonding. Notice in **17.22** that the a_2'' orbital has only metal p character. If the axial–M–axial angle is decreased from 180°, then metal yz can mix into this molecular orbital and this will be a powerful driving force for distortion. The most obvious way to do this is along the Berry pseudorotation coordinate going from **17.19** to the square pyramid **17.18**. Indeed, the first two entries in Table 17.1 are examples, as well as, the TaR_5 compounds mentioned previously.

But what about bending the two axial ligands in the opposite direction, toward one of the equatorial ligands to give a C_{2v} structure, **17.23**? In fact, this structure is

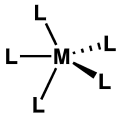

17.23

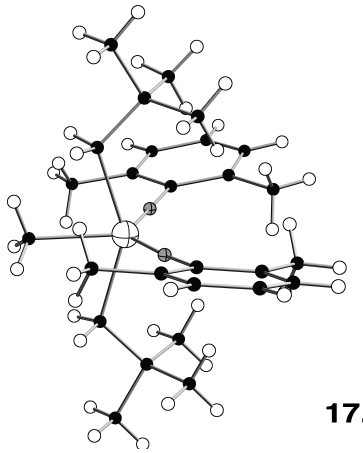

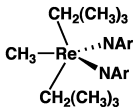

17.24

computed to be the transition state for apical-basal exchange in TaH_5 and $TaMe_5$ [15]. These two molecules are square pyramids in their ground states, and are much more stable than the trigonal bipyramid. Ward and coworkers have elegantly examined what electronic factors can be used to stabilize structure **17.23** [16]. π donors that are oriented so that their *p* AOs lie parallel to the axial–metal–axial axis will be stabilized by the empty metal *xz* and *yz* orbitals. When the two axial ligands are bent back, then the *yz* orbital mixes with metal *z* to produce an orbital hybridized toward the two π donors, and consequently, the latter are stabilized more. A real example (and there are several [16]) is given by **17.24** [17]. There are three anionic alkyl groups along with two imido groups that are counted as having -2 charge. **17.24** is then $Re^{7+} - d^0$. The axial C–Re–C angle is only 147.7°. A d^1 or d^2 (low spin) complex from the examination of Figure 17.3 must be a square pyramid. Two d^2 examples are given in Table 17.1, and d^1 $Mo(CH_3)_5$ [16] is another. A high spin d^2 complex is expected to be a trigonal bipyramid with the $(e'')^2$ configuration. Figure 17.3 indicates that for d^3 and d^4 complexes, the trigonal bipyramid should be favored even more since the *yz* component of e'' rises in energy on distortion away from this structure. There are many examples of d^4 compounds that show this, for example, several $MnCl_5^{2-}$ salts. For d^5 and d^6, a square pyramid (with $\theta \sim 90°$ from Figure 17.3) is expected. For d^7, we need to weigh a two-electron stabilization along the $D_{3h} \rightarrow C_{4v}$ coordinate against a one-electron destabilization. The D_{3h} geometry, however, is Jahn–Teller unstable. In low temperature matrices where low spin d^5, d^6, and d^7 pentacarbonyls have been made [18], these compounds have square pyramidal geometries. The d^6 case is particularly interesting since the level pattern for the D_{3h} and C_{4v} structures suggests the singlet and triplet states might have different geometries. The situation therefore is very similar to that for cyclobutadiene in Chapter 12 and just like the tetrahedral/square planar problem discussed for four-coordinate d^8 molecules in Chapter 16. The d^6 singlet state is unstable at the D_{3h} geometry since the e' orbital would be half-full but is stabilized on distortion to a C_{4v} or C_{2v} geometry. Computations [19] have shown that the C_{4v} square pyramid is the most stable singlet for $M(CO)_5$ where M = Cr, Mo, and W and $\theta = 90.8°$–$89.6°$. This is also consistent with the two experimental structures cited in Table 17.1. A D_{3h} trigonal bipyramid has been computationally found to be stable for the triplet state [20] that lies about 15 kcal/mol above the singlet C_{4v} state. Molecules with a d^8 or d^9 configuration exist either as trigonal bipyramids or square pyramids with plenty

in-between that define the Berry pseudorotation pathway (**17.18** to **17.19**)[21]. In other words, there is a very soft potential associated with this at, especially the 18 electron, d^8 count so that the structure in the solid state is set by inter- and intramolecular nonbonded contacts.

The substitution of one group for another in a molecule is a ubiquitous reaction in chemistry. In the transition metal/organometallic worlds, this most often requires a prior dissociation of a coordinated ligand and then rapid attack of an external nucleophile. The dissociative step may be thermally or photochemically activated. In this context, the photolysis of $M(CO)_6$, M = Cr, Mo, and W, to yield $M(CO)_5$ is of fundamental importance. There is a beautiful collaboration between ultrafast spectroscopy [22] and theory [9,23], which has considerably expanded our knowledge of this reaction. We shall review the situation for M = Cr, which for Mo and W is quite similar. Recall that $Cr(CO)_6$ is a d^6 molecule, so the HOMO (see Figure 15.1) is t_{2g}. The LUMO is not $2e_g$; the CO π^* sets will lie at lower energy. These transform as $t_{1u} + t_{2u} + t_{1g} + t_{2g}$ where all but the last are nonbonding with respect to the metal. On the other hand, $2e_g$ is strongly Cr–C antibonding. So, the lowest excited state is one where an electron from t_{2g} is promoted to the t_{1u} set of CO π^*[24], which has the electronic state symmetry $^1T_{1u}$. This is shown on the left side of Figure 17.6. This is called a metal to ligand charge transfer (MLCT) state. This state, along with

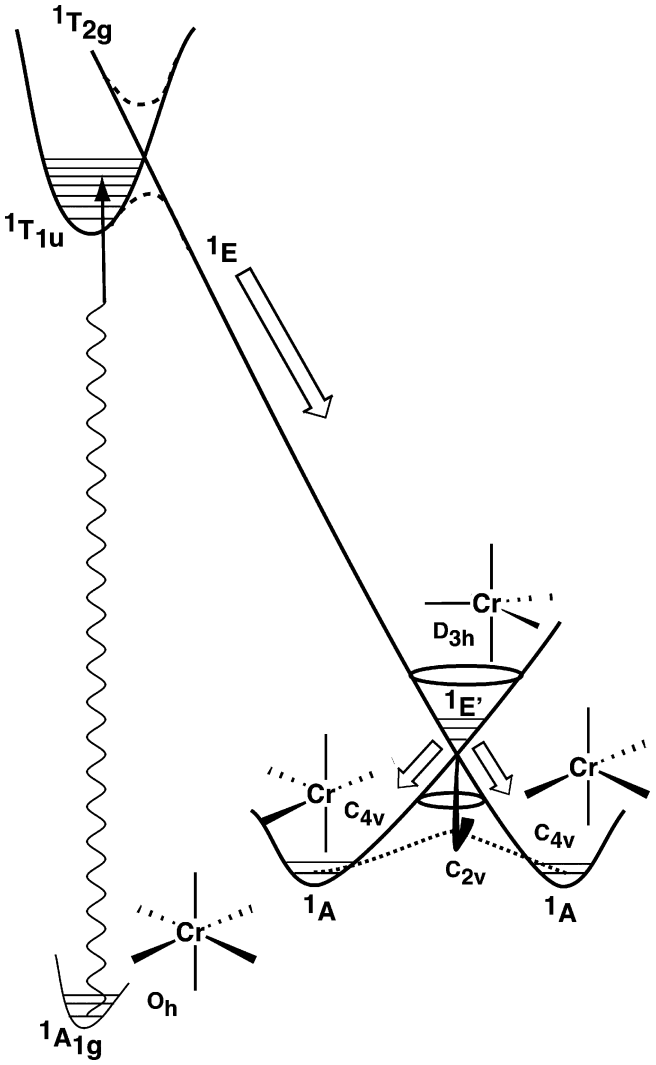

FIGURE 17.6
An electronic state correlation diagram for removing one carbonyl ligand from $Cr(CO)_6$. The vertical energy axis is not drawn to scale.

other MLCT states, is bound with respect to Cr–CO dissociation. Promotion of an electron from t_{2g} to $2e_g$, however, produces a strongly dissociative $^1T_{2g}$ electronic state. A distortion to C_{4v} by removing a CO ligand allows the formation of an avoided crossing between the two states (both have E symmetry). At an excitation of 270 nm, the lifetime of the $^1T_{1u}$ state was measured to be 12.5 fs. There are in fact other MLCT states that also undergo this crossing with very similar lifetimes. The strongly dissociative state of ^{1}E symmetry has a lifetime of 18 fs and ejects the carbonyl ligand with a mean square velocity of about 1200 m/s! The $Cr(CO)_5$ molecule falls into a Jahn–Teller unstable cone ($^1E'$) where it has D_{3h} symmetry and a lifetime of 40 fs. Finally, it passes through the conical intersection to the square pyramidal C_{4v} ground state (^{1}A). But, the dynamics do not stop here. The surface on the lower right of Figure 17.6 is the familiar threefold Jahn–Teller surface, which we encountered in Figure 7.7. The potential surface for the thermal rearrangement of this molecule is similar in form to that for H_3^- and $C_5H_5^+$ described earlier. An idealized representation of it is given in **17.25**. When the $Cr(CO)_5$ molecule is at the Jahn–Teller unstable D_{3h} geometry, it can distort in three ways to form structures A, B, or C in **17.25**. There is more than enough

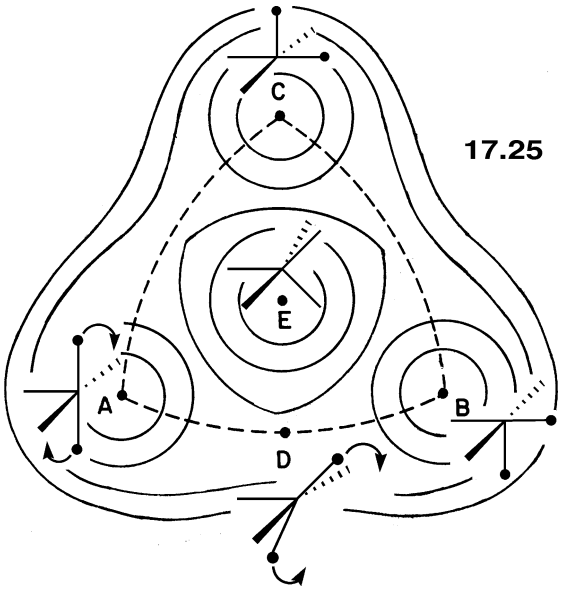

17.25

kinetic energy to send, let us say the molecule in structure A, to structure B. However, it does not do so via the least-motion path that would climb back to the trigonal bipyramid, E. As the arrows associated with A show, there is a peculiar bending motion that sends $Cr(CO)_5$ to a structure with C_{2v} symmetry, D. The C_{2v} structure has been calculated to lie 9.3 kcal/mol above the C_{4v} minimum [9]. The D_{3h} species is 23.1 kcal/mol above C_{4v} [9]. The $M(CO)_5$ molecules are very strong electrophiles that only can be studied in the gas phase or at low temperatures in an inert matrix. There are, however, a growing number of d^6 molecules that are more robust. The important fact is that, unless they are triplets, they will behave in an analogous fashion, avoiding the D_{3h} geometry. Table 17.1 presents two examples. Here, structures A, B, and C are minima and D along with the two other symmetry related structures are transition states. Can this be reversed? Indeed, there are several ways to do this and the interested reader is directed elsewhere for the electronic dissection of this coordination geometry [25].

As mentioned previously within the same molecule, there are two symmetry inequivalent linkages (and therefore sites), axial and equatorial in the trigonal bipyramid (**17.15**) and apical and basal in the square pyramid (**17.14**). The patterns for π bonding [5] can be constructed following the procedure used for the octahedron. For the trigonal bipyramid, there are four symmetry-allowed interactions shown in **17.26**–**17.29**. Three involve interaction with the e'' orbitals and one interaction with the e' orbitals (see the left side of Figure 17.4). **17.28** and **17.29** are equivalent by symmetry. Since the e' orbitals are hybridized away from the ligands as described above and shown in **17.20**, the π-type overlap of a ligand orbital with e' in **17.26** is significantly larger than any of the other interactions, that is, $eq_{\perp} > eq_{||} \gg ax$. However, it is important to realize that

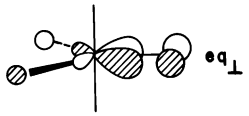

17.26

17.27

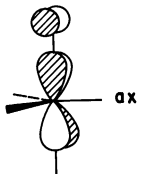

17.28

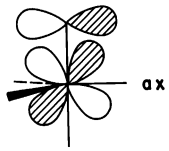

17.29

just because the $eq_{\perp}$ interaction is larger than ax, π-bearing ligands will not always prefer the $eq_{\perp}$ site. The site preferences depend on the number of electrons and on whether the ligand is a π acceptor or donor. For a π acceptor ligand, a d^8 system will prefer the $eq_{\perp}$, and d^2 systems, the $eq_{||}$ arrangement. An example of the d^8 case is provided by the molecule $Ru(PPh_3)_2(CO)_2CF_2$ (**17.30**) [26] . The CF_2 carbene ligand has an empty p AO—a superlative π acceptor orbital orthogonal to the CF_2 plane.

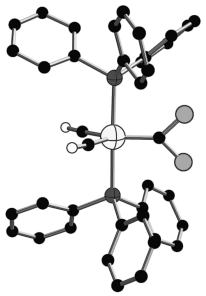

17.30

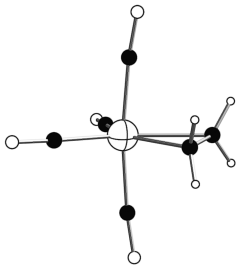

17.31

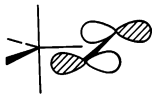

17.32

Therefore, the carbene is oriented in a sterically most demanding position to take advantage of the interaction shown in **17.26**. Another example is provided by $Os(CO)_4$(ethylene)[27], **17.31**, where the ethylene ligand is a π acceptor via its π^* orbital, **17.32**. In fact, all d^8 (olefin)ML_4 complexes have this conformation. We shall explore the consequences of this further in Chapters 19 and 21. An interesting molecule is provided by **17.33** [28]. Each imido group has a formal charge of -2 so we have a d^2 molecule. The imido p AO lone pairs will push the xz orbital of what

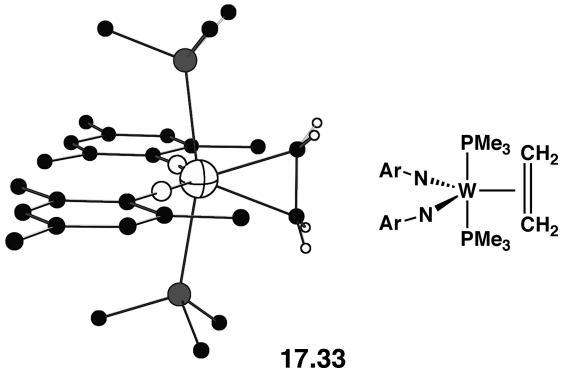

17.33

was the metal e″ set (see the left side of Figure 17.4) above *yz*. Therefore, metal *yz* is filled and will interact with the empty π^* orbital on ethylene as long as the olefin is oriented in the $eq_{||}$ direction. Consider another carbene complex, **17.34** [29].

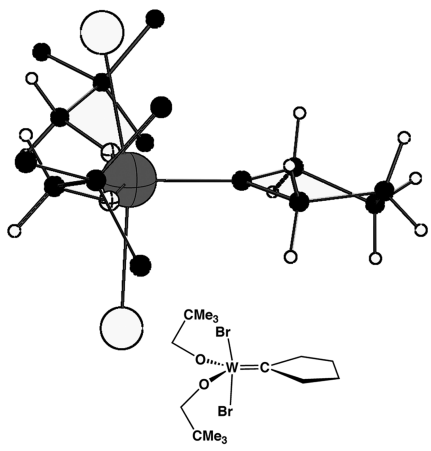

17.34

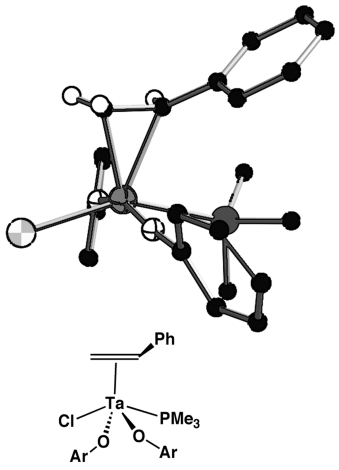

17.35

This is formally a W^{4+} – d^2 system, if the CR_2 carbene group is treated as a neutral two-electron donor with an empty *p* orbital, a superlative π acceptor along the lines of **15.21**. This again presupposes a trigonal bipyramidal geometry and that the *yz* component of e″ on the left side of Figure 17.4 is filled and significantly stabilized with respect to the *xz* component. Another way to view **17.34** would be the carbene has both the σ orbital and the *p* AO filled. It then is an di-anionic fragment yielding a d^0, W^{4+} complex. After all, this is an early transition metal and the carbene complexes in this area are decidedly nucleophilic at carbon as opposed the electrophilic ones represented by **17.30**. But, recall that d^0 molecules are square pyramids rather than trigonal bipyramids. The Br–W–Br angle is 167°—not too far from what is expected for two axial groups in a trigonal bipyramid, but the O–W–O angle is opened much wider than the expected 120° to 159°. Thus, **17.34** could easily be viewed as a square pyramid with the carbene ligand at the apical site and $\theta \sim 98°$. A related example with an olefin at the apical position is given by **17.35** [30]. Here, the Cl–Ta–P angle is 151° and the O–Ta–O angle is 159°. Referring back to the lower left side of Figure 17.3, notice that *xy*, *xz*, and *yz* are close in energy. In **17.34** (using the *xz* plane to correspond to the plane of the paper), *xy* and *yz* orbitals at the metal will overlap with the lone pair π donor orbitals at the two alkoxides ligands and be destabilized. That leaves metal *yz* as the orbital to overlap with the carbene *p* AO. The same affair occurs in **17.35**. The

alkoxides use *xy* and *xz* for π bonding that leaves the filled *yz* orbital to backbond to the olefin π^* orbital. Two unequivocal cases of square pyramidal coordination are given by **17.36** [31] and **17.37** [32]. In **17.36**, $OVCl_4^-$, the oxo group is counted as di-anionic,

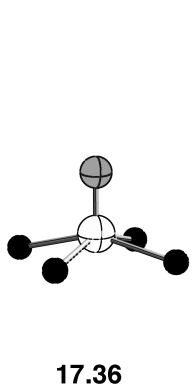

17.36

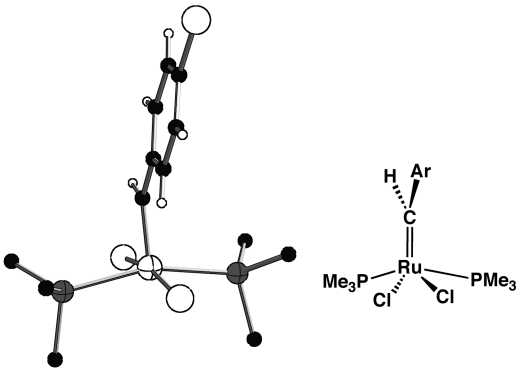

17.37

so this is a d^0 complex with oxygen in the apical site. It uses the two-oxygen *p* AOs to π bond to metal *xz* and *yz*. **17.37** has a d^6 Ru^{2+}, so the electron count is set at 16, the same as in $Cr(CO)_5$ that we have just discussed. The P–Ru–P angle was 161° while the Cl–Ru–Cl angle was 168°. **17.34**, **17.35**, and **17.37** illustrate cases where the π acceptor orbital is in the apical position and is orthogonal to the basal–metal–basal plane that contains the stronger set of π donors. As a consequence, there will be a barrier to rotate the apical group about the metal-apical axis.

17.4 MOLECULES BUILT UP FROM ML_5 FRAGMENTS

In this section, the valence C_{4v} ML_5 fragment orbitals are used to build up the orbitals of more complex units. First, we look at the level structure [33,34] of a simple dimer, M_2L_{10} (**17.38**). The ML_5 *d* orbitals neatly partition into σ (z^2), π (*xz*, *yz*), and δ (x^2-y^2, *xy*) types in this geometry. The details of the resulting orbital diagrams, however,

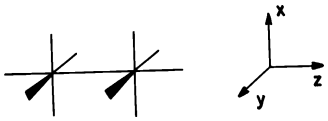

17.38

depend crucially on the identity of the ligands L. Let us look at the two cases, L = Cl and L = CO, typical simple π donor and acceptor ligands, respectively. Recalling that π donors destabilize and acceptors stabilize the "t_{2g}" orbitals (Chapter 15) and that although *xy* may interact with four ligand π orbitals, *xz* and *yz* may only interact with three, we end up with a two above one level arrangement for $M(CO)_5$ and a one above two arrangement for MCl_5. These are shown at the middle of Figure 17.7. The x^2-y^2 level is at very high energy being destabilized by the four basal ligands and is not shown in this figure. Since *xy*, *xz*, and *yz* are destabilized by the lone pairs on Cl, these levels are energetically closer to the z^2 hybrid orbital for $ReCl_5^{2-}$ than in $Re(CO)_5$. These factors are important in understanding the differences in the orbital pictures that result when two MCl_5 or two $M(CO)_5$ units are brought together. The metal–metal distance in $Re_2(CO)_{10}$ of 3.04 Å is much longer than the corresponding distance (2.22 Å) in $Re_2Cl_8X_2^{2-}$ (X = H_2O). As a result, all of the metal–metal interactions are stronger in the halide. Because of this fact and the other points we have just noted, d^7 $Re_2(CO)_{10}$ has a single σ bond between the two metal atoms but $Re_2Cl_8X_2^{2-}$ has a quadruple bond

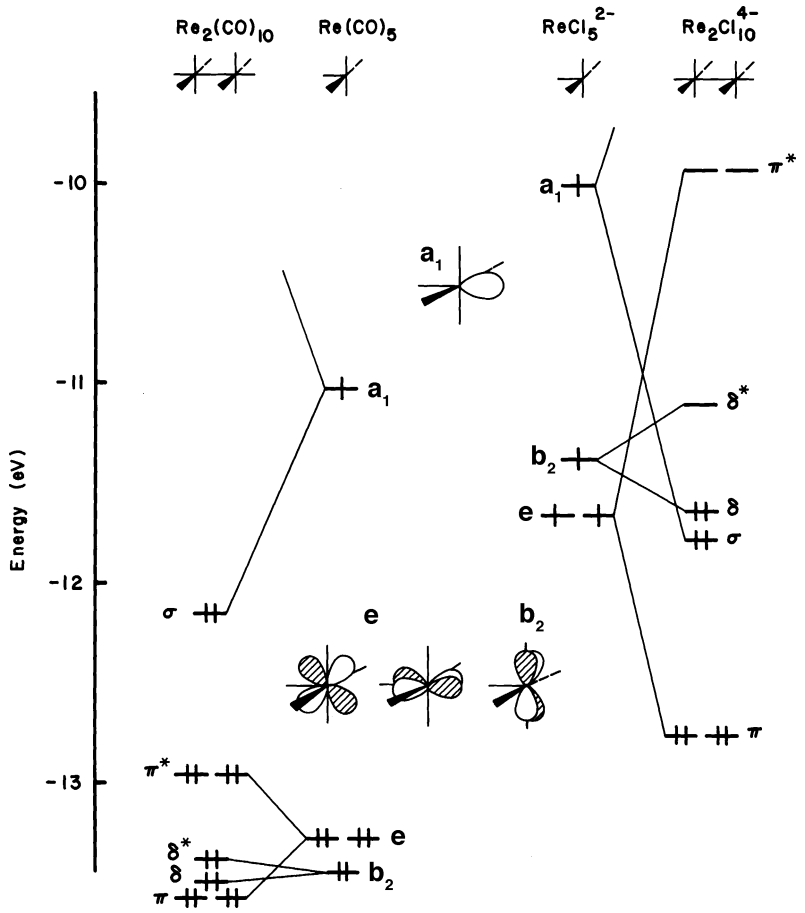

FIGURE 17.7

Interaction diagrams for two M_2L_{10} systems. Notice how the π levels in $Re(CO)_5$ lie lower energy than in $ReCl_5^{2-}$, a direct result of the π acceptor and donor nature of the ligands, respectively. Combined with a shorter metal–metal distance in the halide, the final-level diagrams are quite different.

made up of one δ, one σ, and two π components as shown in Figure 17.7. Just how close do the extended Hückel calculations in Figure 17.7 correspond to the experimental situation? The photoelectron spectrum for $Re_2(CO)_{10}$ is shown in **17.39** [35,36].

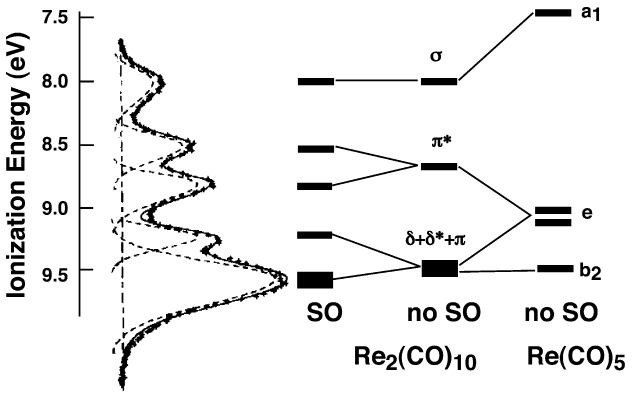

17.39

On the right side are the approximate ionization potentials for a $Re(CO)_5$. These are then split in the same manner as in Figure 17.7 to generate the δ, δ^*, π, π^*, and σ MOs. An important detail is that the π and π^* orbitals are further split into two by spin–orbit coupling effects. This can be analyzed [35] along with other examples containing the $Re(CO)_5$ group to give the fitting in **17.39**. The peak with largest ionization potential is

comprised of δ, δ^*, and the lower component of π. It has roughly three times the area of the other four peaks. The bonding picture in Figure 17.7 closely matches that in **17.39** with the exception that the orbital energies from the calculation are about 4 eV lower than those given by Koopmans' theorem from experiment. How can we increase the bond order between the two ML_5 fragments for the case of L = acceptor? By shortening the M–M distance, the relevant orbitals change in energy in the obvious way shown in **17. 40**. For the case of 10 electrons (a d^5 metal), a formal triple bond is predicted ($\pi^4\delta^2\delta^{*2}\sigma^2$). Indeed, $Cp_2M_2(CO)_4$ species (M = Cr, Mo, W),

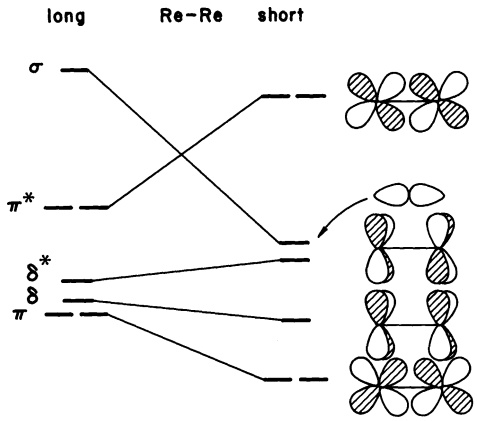

17.40

isoelectronic with the unknown $V_2(CO)_{10}$ molecule, with this electron configuration have very short metal–metal distances. As we will see later Cp is equivalent to three coordinated ligands.

There are a number of molecules having the formula $H(ML_5)_2$, where M = a d^7 metal, that pose an interesting structural feature. One might think of them as being derived from reacting the 18 electron $H–Cr(CO)_5$ molecule, for example, with the 16 electron $Cr(CO)_5$ to give **17.41** [37], which in this case contains a linear Cr–H–Cr bonding arrangement. One might consider this as being the interaction of

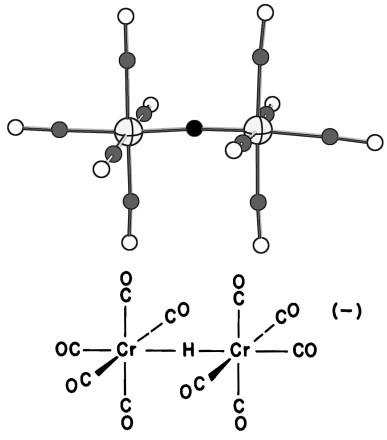

17.41

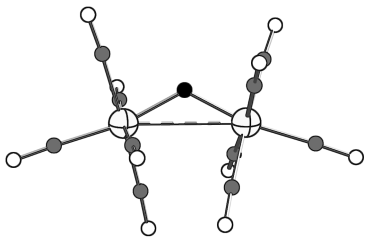

17.42

a Lewis base (the hydride portion of the molecule $HCr(CO)_5$) with the Lewis acid, $Cr(CO)_5$. These compounds can also be prepared by protonating the M–M σ bond in M_2L_{10} dimers. A structural analog, $HW_2(CO)_{10}^-$, is shown in **17.42** [38]. Here, the W–H–W angle is 123.4° and there are, in fact, many isoelectronic compounds with intermediate M–H–M angles. In both cases, we have a three-center–two-electron bond; **17.41** is certainly an example of an "open" one, but then is **17.42**

an example of a "closed" three-center–two-electron bonding arrangement like we have seen many times before in previous chapters? The point of contention here is whether there is metal–metal bonding or not in molecules where the M–H–M bond angle is acute [39]. The energy levels of a linear $H(ML_5)_2$ complex may be derived in a very simple way by adding the hydrogen 1s orbital to the orbital picture produced by the two a_1 orbitals of the ML_5 units set at a very long metal–metal distance expected in a molecule of this type. In other words, this is just the symmetry-adapted combination of the two a_1 hybrids. The hydogen *s* AO will form a bonding and antibonding combination with the symmetric member to form the σ and σ^* MOs in **17.43**. The antisymmetric combination of a_1 hybrids stays nonbonding. There are two electrons, so the σ MO is the only one filled of the

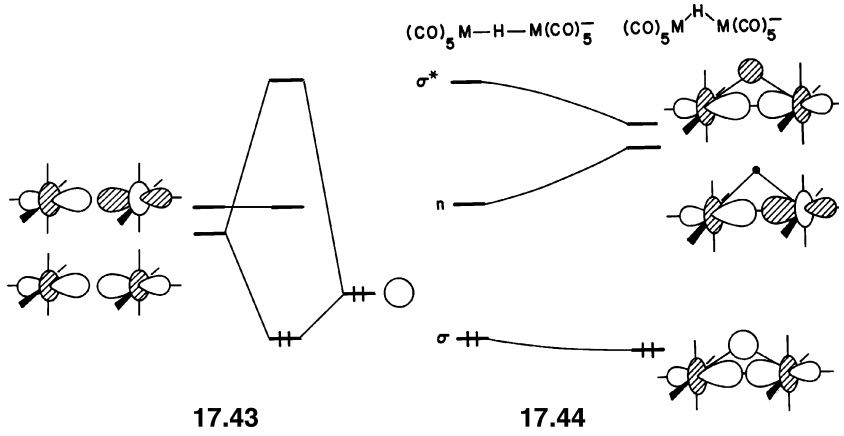

17.43 **17.44**

three. The simplest way to view the distortion leading to a structure like that in **17.42** is to gradually move the metal atoms closer together (and thereby increase their interaction) and, at the same time, move the hydrogen atom off the M–M axis. The result is shown in **17.44** for the pertinent orbitals. The unoccupied out-of-phase z^2 orbital combination (metal–hydrogen nonbonding) goes to higher energy as the metal atoms increase their overlap, and the corresponding bonding combination experiences stabilization. At the same time, however, the hydrogen 1s orbital moves toward a node in the ML_5 z^2 hybrid orbital and overlap is reduced. These two factors operate energetically in opposite directions. This means that the bending motion is rather soft, and a variety of geometries are observed. If the distortion **17.44** proceeds further, the orbital pattern and bonding picture becomes very similar to that of triangular H_3^+ (Section 5.2) and other "closed" three-center–two-electron species. But, there are other arguments as to why the M–H–M bending potential is so soft and there are electron density portioning schemes that shed doubt on the existence of metal–metal bonding [39]. We should make it clear that the argument for the existence of M–M bonding does not imply a bond order of two-thirds, which must be the case in H_3^+, but rather that there is some evidence for an attractive M–M interaction. The W–W distance in **17.42** is indeed quite long—3.34 Å. The W–W distance in the linear $(CO)_5W$–$W(CO)_4$–$W(CO)_5^{2-}$ molecule which has a W–W bond order of one-half, is considerably shorter, 2.79 Å. (The reader should note that the two end $W(CO)_5$ units have symmetric and antisymmetric combinations of the a_1 hybrids like that in **17.43**. The middle $W(CO)_4$ fragment has only an empty z^2 orbital that can interact with the symmetric a_1 combination. The bonding MO is filled and the other two are empty.) As illustrated in **17.44**, if M–M bonding is turned on then the axial C–M–H angle should be less than 180°. In **17.42** it is 169.0°, whereas in **17.41** it is 175.8°, close to the expected 180°. Perhaps more persuasive for the existence of some, albeit small, W–W bonding in

17.42 comes from a series of structures given by **17.45**. The W–W distance varies from 3.37 to 3.12 Å for A = Ge, Si, and C. These molecules also can be considered

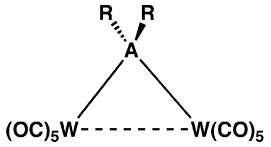

17.45

to have three-center–two-electron bonds (this is a bit of an over-simplification since the *sp* hybrid of the AR_2 group acts in the same way as the *s* AO of H but the empty orthogonal *p* AO on AR_2 can form a bonding combination to the antisymmetric combination of the two *yz* orbitals) and their W–W distances fall within the range given by **17.42**. What is consistent with some W–W bonding in these molecules is that the addition of two electrons makes the W–W distance much longer. It was found to be 4.61 Å when $AR_2 = PH_2^-$ and 4.84 Å for $AR_2 = I^-$. The question of a bond or no bond is almost as old as chemistry itself. Often, these arguments generate more heat than light. We take a perhaps more liberal rather than absolutist view of these matters.

Another problem that may be tackled in the same way as the bridging hydride case is that of a bridging halide that contains *s* and *p* orbitals. Figure 17.8 shows a diagram, analogous to **17.43** for this particular case. Now, both symmetric and antisymmetric z^2 hybrid combinations of the two ML_5 units find suitable partners on the bridging halide. The diagram has been constructed to emphasize the larger σ- than π-type interactions in this unit. The scheme shown in Figure 17.8 gives rise to a collection of six closely spaced orbitals derived from weak π overlap of the "t_{2g}"

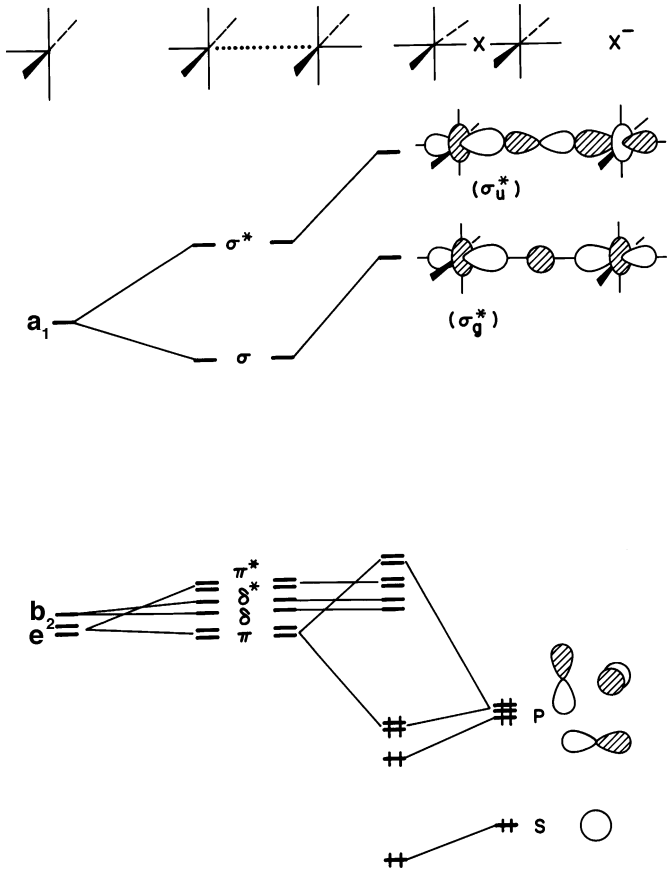

FIGURE 17.8

Generation of the level diagram for an XM_2L_{10} species by allowing the valence *s* and *p* orbitals of X to interact with the orbitals of the M_2L_{10} unit.

orbital sets of the two square pyramids with the bridging ligand orbitals. Two d^4 metals, with a total of eight electrons occupying this collection of six orbitals, are then expected to lead to a paramagnetic situation. If the π interaction between the ML_5 units and the bridging ligand is large, then the situation changes. The result is a much stronger destabilization of the $(ML_5)_2$ level labeled π than shown in the middle of Figure 17.8. With a total of eight *d* electrons, a sizable HOMO–LUMO gap opens up and a diamagnetic species is formed. This is the case [40] for the molecule $Cp(CO)_2Cr–S–Cr(CO)_2Cp$, isoelectronic with $(CO)_5Cr–S–Cr(CO)_5$. The good π contribution to the Cr–S linkages suggests the description $Cp(CO)_2Cr{=}S{=}Cr(CO)_2Cp$ for this molecule.

Sometimes, in these XM_2L_{10} units, the M–X–M bridge is linear; otherwise, it is bent. We are particularly interested in a different type of distortion, the distortion of the symmetric structure to an asymmetric one by slipping the bridging halide towards one of the metal atoms. We have already discussed this type of distortion in the solid state for d^0 metal-oxide compounds where the bridging oxygen atom slips closer to one metal. This is because M–O π bonding is enhanced, see **15.68**–**15.73**. In the following discussion, we concentrate on bridging halides where π bonding is considerably weaker. Examples of this are molecules of the type M_2X_{11}, **17.46**. $Ti_2F_{11}^{3-}$ is a

17.46

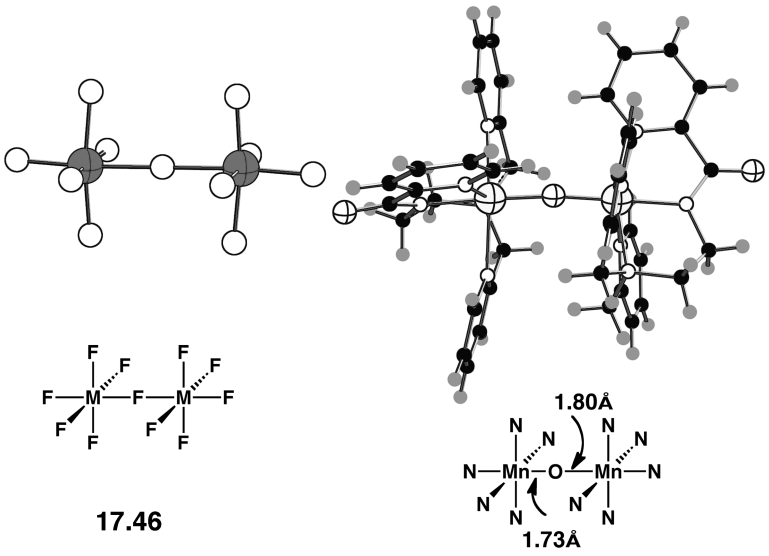

17.47

d^0–d^0 dimer and the bridging fluorine atom is symmetrically placed with Ti–F distances of 1.97 Å [41]. This is the structure observed for $Cr_2F_{11}^{3-}$ (Cr–F = 1.92 Å) [42], which is high spin d^2–d^2 (δ, δ^*, and π^* filled with one electron in each MO in Figure 17.8). $Cr_2F_{11}^{5-}$ (Cr–F = 1.90 Å)[43], high spin d^3–d^3 (δ, δ^*, π^*, and π filled), along with many other metal halide dimers are also symmetrically bridged. Unfortunately, $Cr_2F_{11}^{6-}$ high spin d^3–d^4, or other isoelectronic M_2X_{11} compounds have not been synthesized. We think that the bridging halide will be asymmetrically bonded to the two metals. A closely related example is given by **17.47** [44]. This is a high spin d^3–d^4 system where the bridging oxygen atom is much closer to the left Mn atom that then might be counted as Mn^{4+}–d^3, so the Mn atom on the right has the +3 oxidation state—d^4. This is one of a number of mixed valence compounds. The orbital occupation here puts one electron in each MO up to and including σ_g^*. This pattern also extends to solid-state polymers. The polymeric analog of **17.46**, CrF_5, is symmetrically bridged with Cr–F distances of 1.95 Å [45]. On the other hand, there are a number of Pt^{2+}/Pt^{4+} salts that have an alternating structure. One example is shown in **17.48** [46] where there are two ethylenediamine ligands around each Pt.

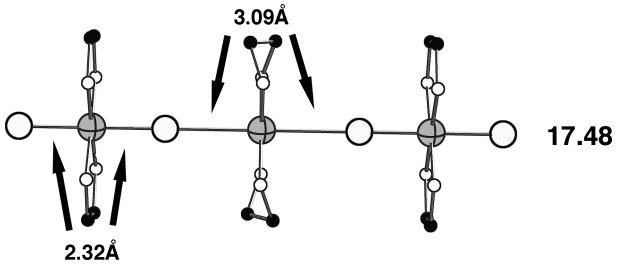

In Section 15.5, we discussed the structure and bonding in d^0 perovskites that have the formula AMO_3 and the idealized structure given in **15.61**. In **17.48**, the orbital occupation corresponds to that in the dimer where there is filling of all MOs through σ_g^*. So, a clue to understanding this particular motion lies in the energetic behavior of the σ_g^* and σ_u^* orbitals of Figure 17.8. It is difficult to predict *a priori* whether σ_g^* or σ_u^* lies higher in energy, but we see that for our purposes it is not important. Let us assume that σ_g^* is lower than σ_u^* at the symmetric geometry, see the middle of Figure 17.9. A Walsh diagram at the extended Hückel level plots here the energies of these two MOs as a function of the Cr-bridging Cl bond distance on the left side, keeping the Cr–Cr distance constant. As the bridging Cl moves to the left or right, the center of symmetry is lost and σ_g^* and σ_u^* orbitals mix together. The top orbital always goes up in energy, and the bottom orbital drops in energy as a result of this orbital intermixing (Figure 17.9). The change in the nature of the σ_g^* and σ_u^* orbitals on distortion is an interesting one [15]. The higher energy orbital at the symmetrical

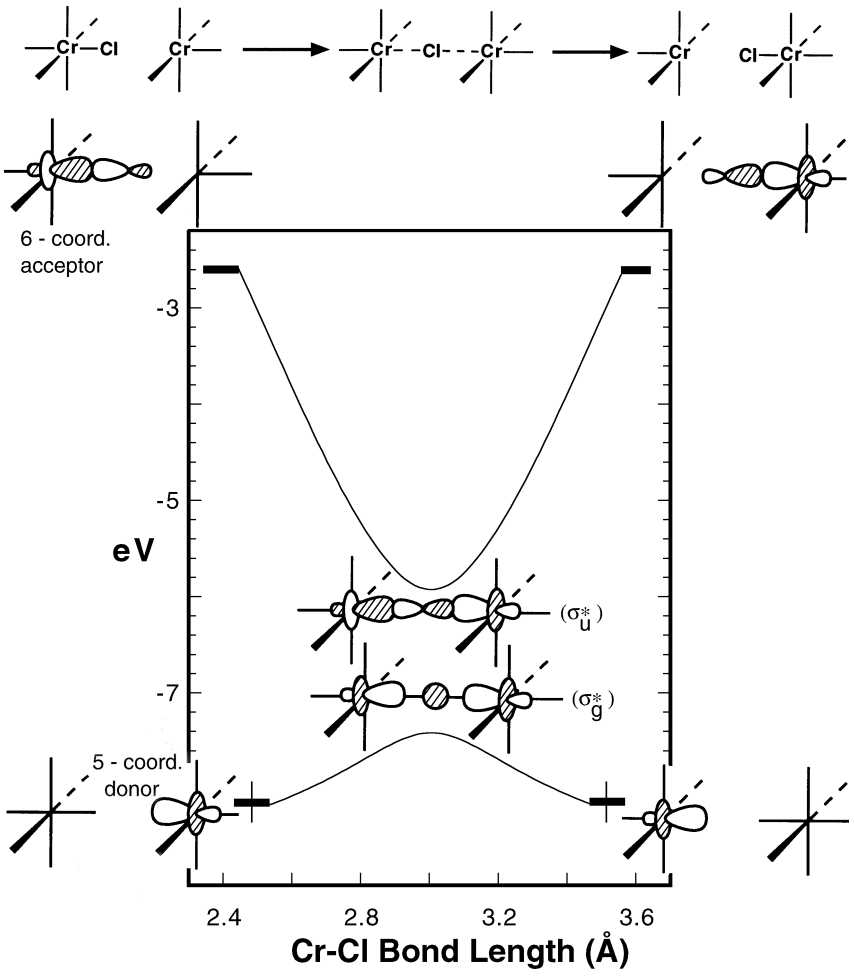

FIGURE 17.9
Walsh diagram at the extended Hückel level for the σ_g^* and σ_u^* orbitals in $Cr_2Cl_{11}^{6-}$ as the bridging Cl atom is moved off center.

structure ends up as a σ antibonding orbital (one of the e_g pair) on the now approximately octahedral unit, and the lower energy orbital becomes a pure z^2 hybrid orbital located on the ML_5 square pyramidal fragment. Figure 17.9 shows this pictorially for both the left and right distortions of the bridging atom or alternatively as the bridging atom is moved from one side of the bridge to the other.

Let us work with the example on the left side of Figure 17.9. As the bridging halide moves toward the metal atom σ_u^* mixes (**17.49**) into σ_g^* in a way to reduce the antibonding interaction between the metal atom on the left and the bridging atom (z^2 in σ_u^* is bonding to the halide *s* orbital in σ_g^* and the halide *z* in σ_u^* is bonding to metal z^2 in σ_g^*). The resultant orbital cancels amplitude on the left ML_5

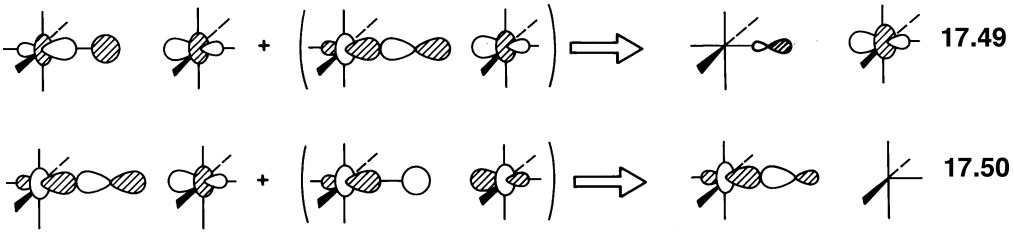

unit and reinforces it on the right ML_5 unit. Now, σ_g^* must mix into σ_u^* with the opposite phase relationships. The result, shown in **17.50**, has reinforced amplitude at the left ML_5 fragment and canceled amplitude at the right ML_5. If σ_u^* lies below σ_g^* in Figure 17.9, exactly the same results are obtained. We shall continue with the ordering of σ_g^* below σ_u^*. With one or two electrons in the σ_g^* orbital, this simple result indicates that such species will be unstable at the symmetrical structure and should distort to the asymmetric arrangement. This is a typical example of a second-order Jahn–Teller distortion. For the case of two electrons, the electronic ground state is $^1\Sigma_g^+$ and the lowest excited singlet state is of symmetry $^1\Sigma_u^+$. The distortion mode that will lower the energy of the system via a second-order Jahn–Teller mechanism is of symmetry $\sigma_g \otimes \sigma_u = \sigma_u$, that is, the asymmetric motion of the central atom. The Mn^{3+}/Mn^{4+} compound in **17.47** with one electron in σ_g^* is one example showing this distortion. With two electrons in the σ_g^* orbital, the classic series of Pt^{2+}/Pt^{4+}-mixed valence compounds are found (**17.48**). Both of these examples are mixed valence compounds because, as we can see from Figure 17.9 at the asymmetric structure, the σ_g^* electron(s) are located on the five coordinate unit in $CrCl_5^{3-}$ (and the analogous orbital for the square planar Pt case).

There are strong links between these mixed valence species and an important class of reactions—namely those arising via electron transfer [48]. The inner sphere redox behavior of the Cr^{2+}/Cr^{3+} system has been studied in great detail. By using labeled chloride (Cl^*), it was cleverly shown that the redox process is associated with atom transfer (**17.51**) and that this occurs in the opposite direction to electron transfer, perhaps via the inner sphere complex (**17.52**). In **17.51**, we use the terms

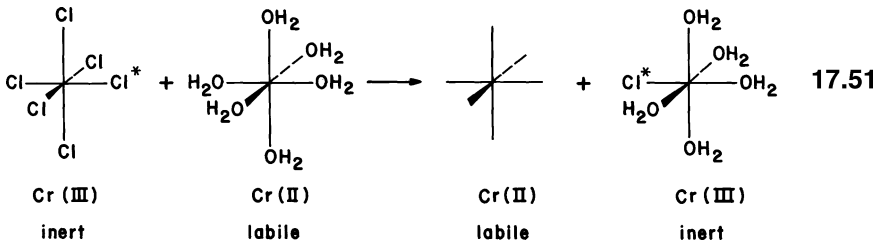

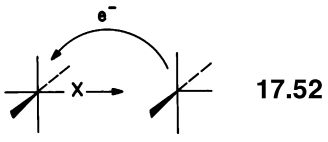

labile and inert to describe the kinetic stability of these complexes. Ligand substitution at Cr^{3+} is very slow, and so, the identity of the $CrCl_5Cl^{*3-}$ ion is preserved in solution. In contrast, ligand substitution at Cr^{2+} is fast, and so, the ion is best described as an aquo complex constantly exchanging water molecules with the solvent. After electron transfer, the coordination sphere around the old Cr^{2+} ion (new Cr^{3+} ion) is frozen since it is now the inert species in solution. The coordination sphere around the old Cr^{3+} ion (new Cr^{2+} ion) will rapidly be replaced by water. We can use the scheme of Figure 17.9 to see how this takes place in detail. On the left-hand side of the diagram, the electron is totally associated with the square pyramidal five-coordinate reductant, Cr^{2+}. As the X atom from the Cr^{3+} unit moves to the center of the bridge (a transition state from our discussion above), the orbital containing this electron has equal weight from both metal atoms. Technically, "half an electron" has been transferred at this point. As the bridging atom moves past the symmetric structure to the right-hand side of the bridge, then the electron transfer is now complete and Cr^{2+} and Cr^{3+} species are again produced. Thus, the electron transfer has proceeded in a smooth way initiated by the atom transfer. We stress that not all redox processes are this simple (many proceed by the outer sphere route where no species such as **17.52** occurs), but within the context of this electronic model, one can think about ways that the other ligands around the metal and the transferred halogen can perturb the rate of the reaction.

As we mentioned above, the Pt^{2+}/Pt^{4+} mixed valence compounds are in fact found as infinite chains. So, instead of the two orbitals, σ_g^* and σ_u^* of Figure 17.8, we have an energy band [49] shown in Figure 15.11. At the symmetric geometry, the z^2 band is just half-full, signaling a Peierls-type distortion. The distortion exhibited in **17.48** requires that the unit cell be doubled so the z^2 band is folded back as shown by the dotted line for the $e(k)$ versus k plot in **17.53**.

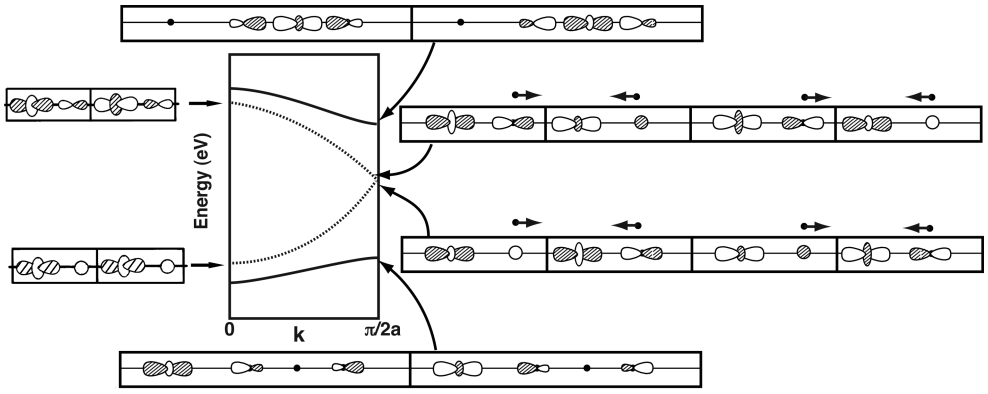

17.53

The $k = 0$ and $\pi/2a$ solutions are explicitly shown. At $k = 0$, the very bottom of the z^2 band corresponds to the σ_g^* type of orbital with a phase factor of $+1$ between adjacent cells, and the top of the z^2 band at $k = 0$ is the corresponding σ_u^* combination. The $k = \pi/2a$ solutions have the form

$$\psi \propto (\chi_1 - \phi_1) + (\chi_2 + \lambda_2) - (\chi_3 - \phi_3) - (\chi_4 + \lambda_4) + (\chi_5 - \phi_5) + (\chi_6 + \lambda_6) + \cdots \tag{17.1}$$

and

$$\psi' \propto (\chi_1 + \lambda_1) - (\chi_2 - \phi_2) - (\chi_3 + \lambda_3) + (\chi_4 - \phi_4) + (\chi_5 + \lambda_5) - (\chi_6 - \phi_6) + \cdots \tag{17.2}$$

where χ, λ, and ϕ represent the Pt z^2, Cl s, and Cl z contributions, respectively, and the subscripts refer to the numbering in the primitive unit cell. Just as the pair of orbitals of Figure 17.9 increased their separation as the bridge is made asymmetric, so the band of the infinite system splits into two on such a distortion. The upper and lower bands mix with each other, stabilizing the latter and destabilizing the former. The phases in **17.53** have been chosen so that the upper band at $k = \pi/2a$ mixes in phase into the lower one. By adding equation 17.2 into equation 17.1, one can easily verify that the z^2 coefficients at unit cell 1, 3, 5, . . . are reinforced and those at unit cell 2, 4, 6, . . . cancel. The lower band, of course, also mixes into the upper one, now out of phase. Subtracting equation 17.1 from equation 17.2 cancels the z^2 coefficients at unit cell 1, 3, 5, . . . and increases them at 2, 4, 6, . . . The reader can easily derive the crystal orbitals at the $k = 0$ point. The lower band has become the filled z^2 combination on the Pt atoms that have long distances to the bridging Cl atoms. The upper band becomes localized on the Pt atoms that have the short Pt–Cl distance. Note that the stabilization results in a square planar environment for low spin d^8 Pt^{2+} and an octahedral environment for the low spin d^6 Pt^{4+} species, two typical geometries for these oxidation states. The application of pressure [50] causes the chains to become compressed. The Pt–Cl distances then become closer to each other, and the conductivity greatly rises.

17.5 PENTACOORDINATE NITROSYLS

Coordinated NO is found in two basic geometries in transition metal complexes, linear and bent, exemplified by the molecules **17.54**–**17.56** [51–53], as well as structures intermediate between the two. We shall concentrate on five-coordinate

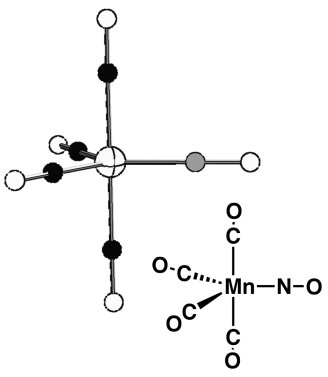

17.54

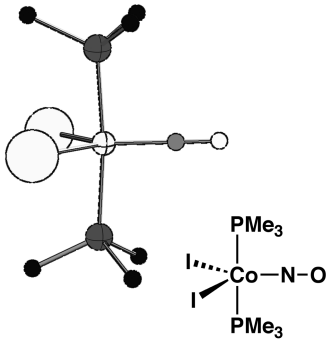

17.55

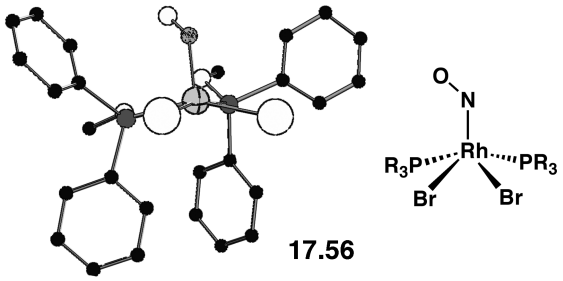

17.56

examples that may have a square pyramidal, trigonal bipyramidal, or an intermediate coordination environment. We are interested in understanding in broad terms when the MNO unit is linear and when it is bent [54,55]. We begin with a square pyramidal ML_4NO complex containing an apical nitrosyl group. Figure 17.10 shows the assembly of such a diagram in the obvious way, using the important frontier orbitals (n, π^*) of the

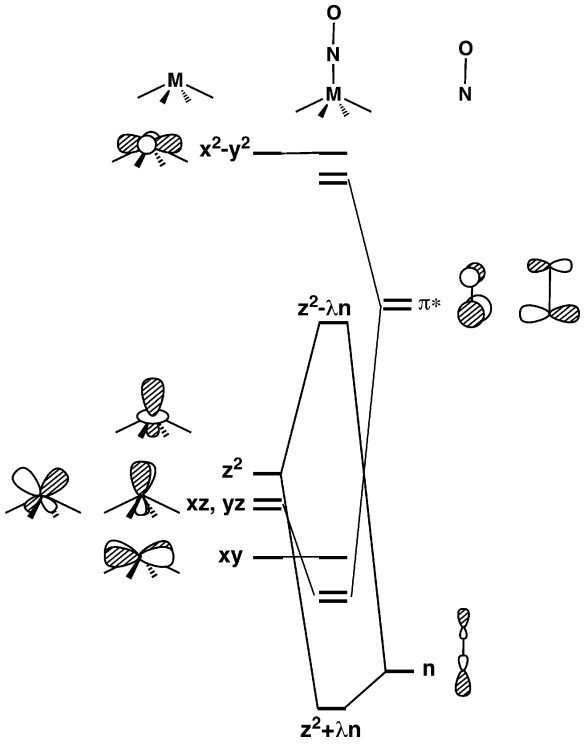

FIGURE 17.10
Construction of the important valence orbitals in a $ML_5(NO)$ molecule.

NO. On the left of Figure 17.10 are the orbitals of a square pyramidal (C_{4v}) ML_4 unit. There are a couple of ways to derive these orbitals. One could start with the *d* orbitals of the square plane—see Figure 16.1 or the left side of Figure 16.4. Making the four ligands pyramidal leaves the *xy* orbital unchanged in energy. It stays totally nonbonding. The $x^2 - y^2$ orbital is stabilized somewhat since some overlap to the ligands is lost. This also occurs in z^2 except that metal *s* and *z* hybridize with z^2 so that the orbital points out away from the ligands. The mechanism for this change is identical to that for pyramidalization in AH_3 (Chapter 6). Finally, *xz* and *yz* are destabilized and somewhat hybridized. A close comparison of the ML_4 orbitals and those of the C_{4v} ML_5 unit on the right side of Figure 17.3 shows that there is only one difference. Removal of the apical ligand in ML_5 stabilizes the z^2 orbital greatly and rehybridization occurs so that it is pointed toward the missing apical ligand. The z^2 orbital is crucial for understanding the bending of NO. It finds a strong interaction with the lone-pair orbital of NO that has been labeled n on the right side of Figure 17.10. Bonding, $z^2 + \lambda n$, and antibonding, $z^2 - \lambda n$, MOs are created. Likewise, *xz* and *yz* interact with the π^* levels of NO to form bonding, $xz/yz + \lambda\pi^*$, and antibonding, $xz/yz - \lambda\pi^*$, combinations. When filling this manifold with electrons, we need to keep track, not only of the number of *d* electrons but in addition those which lie in the nitrosyl π^* levels. The sum of the two (*m*) is given by a notation $\{MNO\}^m$. Figure 17.11 shows how the energy of these levels change as the MNO angle decreases from 180°. The $z^2 - \lambda n$ level is stabilized quite dramatically. As shown in **17.57**, there are two effects behind this.

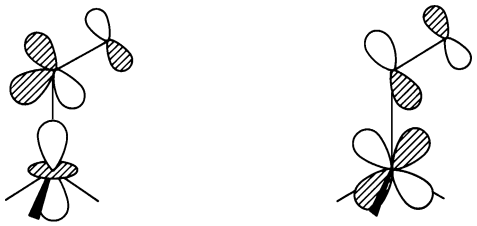

17.57 **17.58**

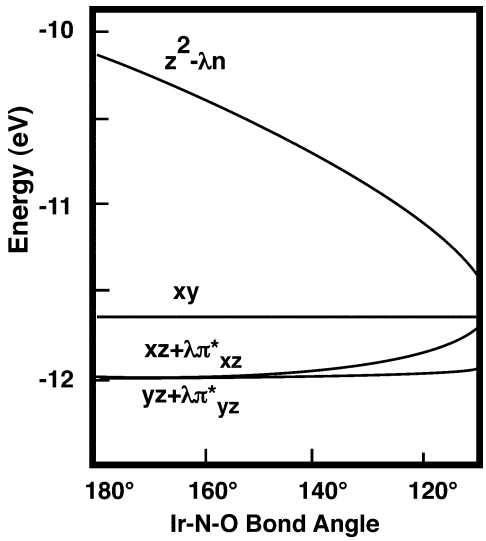

FIGURE 17.11

Energetic behavior of the metal *d* and nitrosyl π^* levels on bending the M–N–O unit. Adapted from Reference [54], the extended Hückel calculation refers to an iridium nitrosyl species.

The antibonding interaction with the nitrosyl lone pair (*n*) is reduced on bending since now M, N, and O are not collinear. Using geometric perturbation theory, this loss of overlap between z^2 and *n* creates a first-order change in energy that is negative. Concurrently, a bonding interaction between z^2 and the nitrosyl π^* orbital is turned on. Within a perturbation theory construct, there is a second-order energy correction between $z^2 - \lambda n$ and primarily $xz - \lambda\pi^*_{xz}$ along with $xz + \lambda\pi^*_{xz}$. The interaction of one component of the nitrosyl π^* orbitals (π^*_{xz}) with *xz* decreases on bending **17.58**, and $xz + \lambda\pi^*_{xz}$ becomes less M–L π bonding and rises in energy, that is, there is a positive first-order energy correction. In a simple way, then, Figure 17.11 indicates two opposing factors influencing bending. Occupation of $xz + \lambda\pi^*_{xz}$ favors linearity but the occupation of $z^2 - \lambda n$ favors bending. There are several $\{MNO\}^4$ molecules. One example is given by **17.59** [56]. Here, the

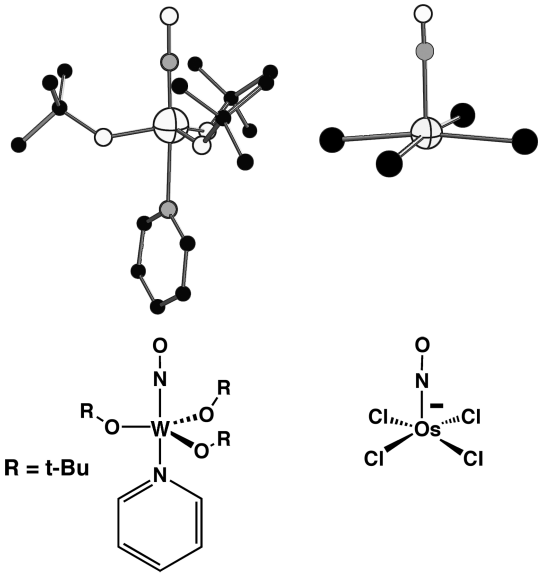

17.59 **17.60**

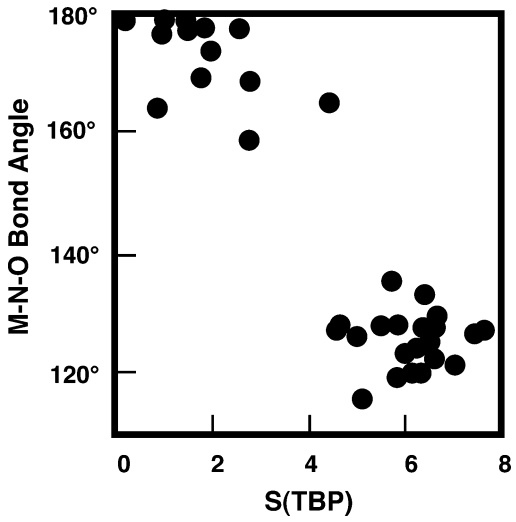

FIGURE 17.12
Plot of the M–N–O bond angle versus the symmetry measure for a trigonal bipyramid, S(TBP) in molecules with a $\{MNO\}^8$ electron configuration. The plot has been adapted from Reference [59].

xz/*yz* $+ \lambda\pi^*$ MOs are filled and *xy* is empty. All of these molecules have linear M–N–O bond angles as expected from Figure 17.11. For $\{MNO\}^6$ systems where *xy* is the HOMO, the approach also definitely predicts a linear geometry. There are a number of molecules that confirm this. One example is provided by **17.60** [57]. Notice that **17.59** is a trigonal bipyramid and **17.60** is a square pyramid in agreement with the Walsh diagram given in Figure 17.4. The placement of the excellent π acceptor ligand, NO, in the axial and apical positions, respectively, allows for maximal stabilization (note that the equatorial groups in **17.59** are bent away from the NO group so as to hybridize the *xz*/*yz* orbitals towards NO π^*). For the $\{MNO\}^8$ configuration $z^2 - \lambda n$ is filled and inspection of Figure 17.11 suggests that bending should occur for the square pyramid. An example is provided by **17.56**. The M–N–O bending potential is drastically reduced, and linear nitrosyl molecules are quite common (see **17.54** and **17.55**) by changing the nature of the coordination geometry to the trigonal bipyramid, which is beyond the scope of our discussion here [54]. Recall that the Berry pseudorotation path for the conversion of the trigonal bipyramid to square pyramid is a soft potential for this electron count. There is way to quantify how far away a molecule is distorted from a trigonal bipyramid (toward a square pyramid)[58]. This is called the symmetry measure, S(TBP), for a trigonal bipyramid. A plot [59] of the M–N–O bond angle versus S(TBP) for $\{MNO\}^8$ molecules is given in Figure 17.12. S(TBP) $= 0$ defines a perfect trigonal bipyramid; however, any structure with S(TBP) $\leq \sim 3$ is close to one. When S(TBP) $\geq \sim 5$, then it is close to a square pyramid. Figure 17.12 shows that molecules with a trigonal bipyramidal geometry have linear M–N–O bond angles or close to it, whereas square pyramids are strongly bent.

17.6 SQUARE PYRAMIDS IN THE SOLID STATE

By far the most common coordination geometry in the solid state is the octahedron followed perhaps by the tetrahedron. Trigonal bipyramids are quite rare, but there are a significant number of materials that are built from square pyramids. In this section, we shall look at three compounds with different electron counts.

V_2O_5 is a solid-state compound with many catalytic and electronic uses including an electrode material for rechargeable lithium batteries. Its structure [60] is

somewhat complicated and has been described in a number of ways. The most useful perspective is that it consists of rows of edge-shared square pyramids, **17.61**, which form a layered structure. There are double rows of "up" and "down" pointed

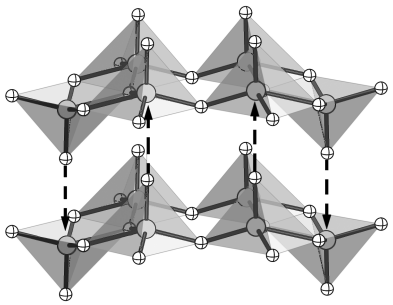

17.61

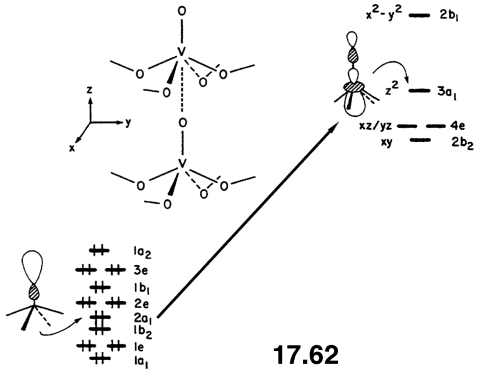

17.62

pyramids, and the registry of the layers is such that the apical oxygen from one layer is directly above or below the vanadium atom in an adjacent layer. The dashed arrows show several of these contacts in **17.61**. The layers in graphite (Section 13.4) are held together by van-der-Waals forces, and it is easy to intercalate materials between the layers. V_2O_5 also can be intercalated by, for example, Li, Na, or K that form a number of vanadium bronzes with varying degrees of electrical conductivity. The interest here is whether or not there remains some covalent bonding between the vanadium atoms in one layer and apical oxygen atoms from an adjacent layer. The distances are 2.79 Å, which are very long. The V–O distances to the basal oxygen atoms range from 1.78 to 2.02 Å, while that to the apical oxygen is even shorter, 1.58 Å. If any covalent interlayer interaction exists, the most likely source would be from the outer-pointing, filled hybrid on the apical oxygen atoms, and the empty z^2 hybrid on vanadium. This is shown in **17.62**. The DOS [61] for V_2O_5 where the layers are separated by a very long 6.00 Å is shown in Figure 17.13a. The states from about −16.1 eV to the Fermi

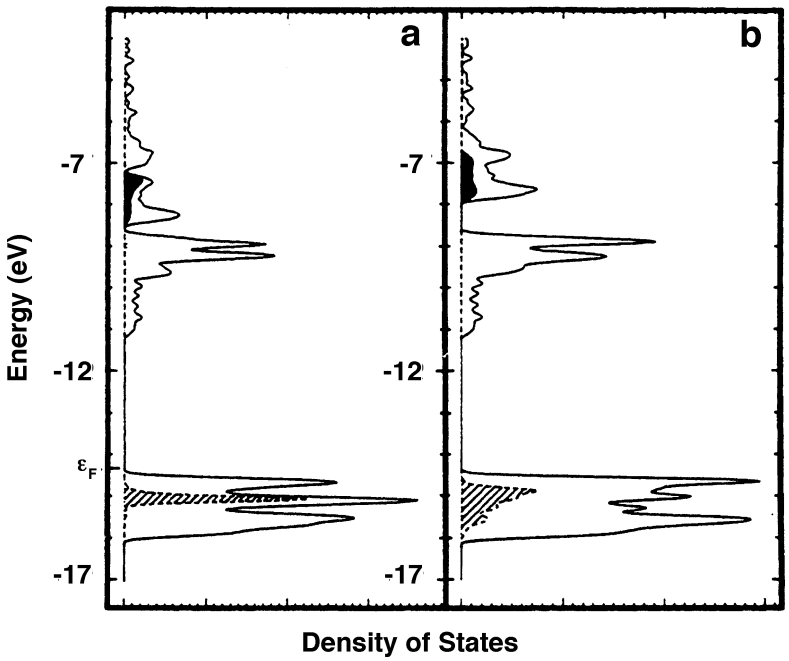

FIGURE 17.13

DOS for V_2O_5 when the distance between the vanadium atoms of one layer and the apical oxygen atoms in an adjacent one is 6.00 Å in (a) and the experimental distance, 2.79 Å, in (b). The projection of the apical oxygen lone pair, $2a_1$, in **17.62** is given by the shaded area. The vanadium z^2 projection is shown by the solid area. The Fermi level is indicated by ε_F. The DOS plots are taken from Reference [61].

level at −14.4 eV correspond to the oxygen *p* AO region. The projection of the apical oxygen z AO is given by the shaded area. The narrow peak is consistent with its nonbonding nature. The region from −11.2 to −8.5 eV consists primarily of vanadium *xy*, *xz,* and *yz* (see **17.62**). The z^2 contribution is found in the dark area from about −7.2 to −8.5 eV. Its dispersion is due to small mixing with the basal oxygen atoms. The $x^2 - y^2$ levels lie above −7.1 eV and are greatly dispersed by σ bonding to oxygen. In Figure 17.13b, the interlayer distance was decreased to the experimental value of 2.79 Å. The states with oxygen *z* character have been stabilized, and there is much greater dispersion. The majority of the vanadium z^2 levels are destabilized. Both of these facets are consistent with the establishment of covalent bonding between vanadium and oxygen. At the extended Hückel level [61], 0.05 electrons were transferred from the apical oxygen to vanadium as a result of this interaction. From an energetic perspective, this is worth 4.5 kcal/mol per vanadium atom. Clearly, this is not a typical V–O single σ bond. One can use the Mullikan overlap population as a gauge. Again, at the extended Hückel level, the V–O basal overlap population was calculated to be 0.389, whereas the interlayer V–O population was 0.064. Coincidently, the V–O overlap population to the apical oxygens within the layer was found to be 0.880. This large value is consistent with the strong π overlap that exists between oxygen *x* and *y* with vanadium *xz* and *yz*.

In 1988, Bednorz and Müller were awarded the Nobel Prize in Chemistry for the discovery of superconductivity in $La_{2-x}Sr_xCuO_4$ with a T_c at 35 K [62]. We have discussed the electronic structure of this material in Section 16.5. Chu and coworkers prepared a related compound, $YBa_2Cu_3O_7$, with a $T_c = 92$ K [63]. The structure of this compound is shown in **17.63**. The environment around Cu1 is clearly a corner-shared square plane that runs along the *x*-axis to form a one-dimensional chain. On either side of this chain in the z direction lies a puckered

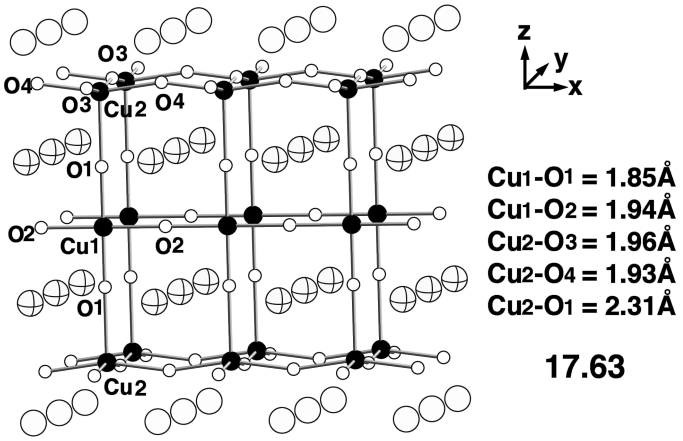

two-dimensional net of CuO_2. Thus, one has a layer of $Cu_3O_7^{7-}$, which is sandwiched on the top and bottom by an Y^{3+} layer, and Ba^{2+} cations are stuffed within the copper-oxide layers. The CuO_2 nets are connected to the square planes via O1. Thus, the Cu2 environment may be regarded as square pyramidal. The basal O–Cu2–O angles were 164.4°, or another way of putting this is that the Cu2 atoms lie 0.32 Å out of the O3/O4 plane. An alternative polyhedral view of this structure is then given in **17.64**. How then should one view the copper oxidation states in the $Cu_3O_7^{7-}$ layers? In principle, there are two possibilities: (1) three $Cu^{2.33+}$ ions or (2) two Cu^{2+} and one Cu^{3+} ions. In other words, are we dealing with a delocalized or

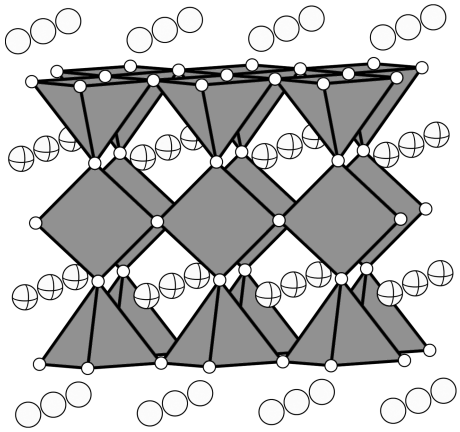

17.64

a mixed valence case? If the latter is true, then one might expect that the Cu1 atoms in the chains are $+3$, d^8, so the copper d bands are filled up to the $x^2 - z^2$ one (see the coordinate system in **17.63**). The Cu2 atoms in the square pyramids then are d^9, so the two $x^2 - y^2$ bands are exactly half-full (for an antiferromagnetic ordering) and present a situation exactly like that for the CuO_2^{2-}plane in Section 16.5. Extended Hückel calculations on $YBa_2Cu_3O_7$ have shown [64] that the latter atomic distribution is indeed appropriate for the equilibrium structure at rest. Density of states plots for the energy region around the Fermi level is presented in Figure 17.14.

The left side shows the projection of the Cu2 $x^2 - y^2$ states where the dashed line corresponds to the copper contribution and the dotted line to the oxygen contribution. The panel on the right side shows the projection of the Cu1 $x^2 - z^2$ states. On average, the Cu2 $x^2 - y^2$ bands lie lower in energy than Cu1 $x^2 - z^2$. The principal reason for this is that since the Cu2 atoms lie out of the plane of the surrounding four oxygen atoms in contrast to the situation for the Cu1 atoms, the σ overlap of the oxygen AOs to Cu2 $x^2 - y^2$ is diminished. As a result the Fermi level, ε_F, in Figure 17.14 lies right in the middle of the Cu2 $x^2 - y^2$ states. So, why should this material become metallic and superconducting when the planar CuO_2^{2-}

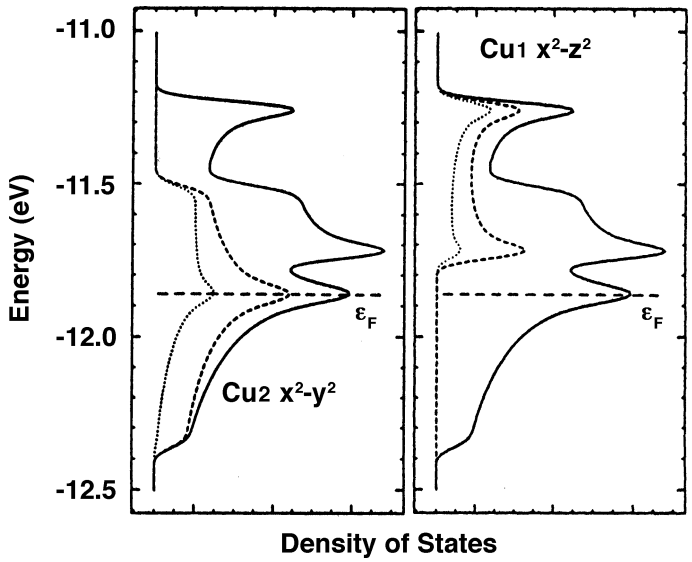

FIGURE 17.14

The density of states for the region around the Fermi level, ε_F, in $YBa_2Cu_3O_7$. The plots show the projection of copper and oxygen character by the dashed and dotted lines, respectively. The plots were adapted from Reference [64].

family needed to be doped with electrons or holes to achieve this condition (see Figure 16.5)? Notice that distance of O1 to Cu1 is very short while that to Cu2 is quite long. One can easily show that moving the O1 atoms along the z axis bringing them closer to the Cu2 atoms will cause the $x^2 - z^2$ states at Cu1 to move to lower energy and become occupied and, thus, the $x^2 - y^2$ Cu2 states become emptied. One could also consider vibrations of the O1 atoms in the *x* or *y* directions to create the same electronic situation. If the Cu2 atoms are displaced into the plane of the surrounding oxygen atoms, then the Cu2 $x^2 - y^2$ states will be raised in energy and again the electronic state moves towards that of the delocalized type for the three copper atoms. The dynamic features of the family of compounds related to $YBa_2Cu_3O_7$ and its impact on superconductivity from a chemist's perspective may be found elsewhere [65].

The structure [66] of $BaNiS_2$ is very similar to that presented for V_2O_5 except, as shown in **17.65**, that there are Ba cations between the NiS_2 layers and consequently there is no interlayer bonding present in this material. The NiS_2^{2-}

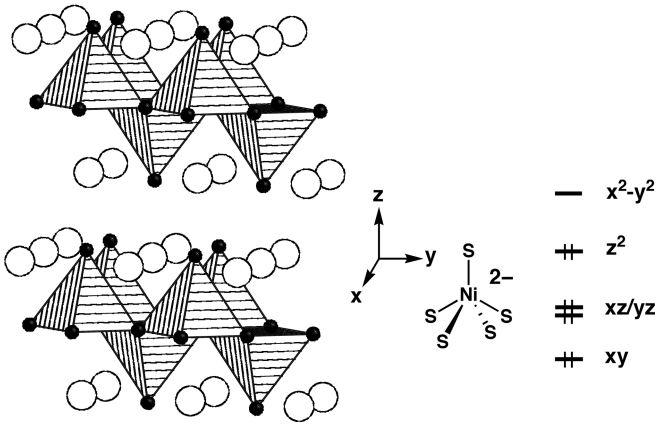

17.65 **17.66**

layer then makes the formal oxidation state of nickel to be +2, which is d^8 in contrast to the d^0 electron count in V_2O_5. There are some important structural differences, as well. The *d* AO splitting for a square pyramid, taken from the right side of Figure 17.4, is reproduced in **17.66**. Since *xz*, *yz*, and z^2 are filled, the Ni–S basal and apical distances are nearly equal, 2.34 and 2.32 Å, respectively. The apical–Ni–basal angle is 109.1° (in V_2O_5, the average apical–V–basal angle is 106.6°). With the electronic formulation in **17.66,** one might think that $BaNiS_2$ is a semiconductor. The $x^2 - y^2$ and z^2 bands will spread out in a typical two-dimensional manner; the issue is to what extent this will occur. In actual fact, $BaNiS_2$ is a metal [66]. The density of states around the Ni $x^2 - y^2$ and z^2 region is presented in Figure 17.15. The dispersion associated with the $x^2 - y^2$ band was discussed in Chapter 16; see **16.49**–**16.51**. The dispersion for z^2 comes about in a very similar manner and is primarily due to differential π overlap with the basal sulfur atoms. The important point is that at the extended Hückel level, the two bands cross. This also occurs at much higher levels of theory [67]. Within this context, the metallic character of $BaNiS_2$ is understandable. One might think that $BaCrS_2$ would be metallic because of the low, d^4 electron count at Cr. This is not the case [68]. With the *d* AO splitting pattern in **17.66**, one might expect that the *xz*/*yz* set would be half filled leading to a metallic state as illustrated on the left side of **17.67**. This is not the case. The structure of $BaCrS_2$ is distorted a good bit

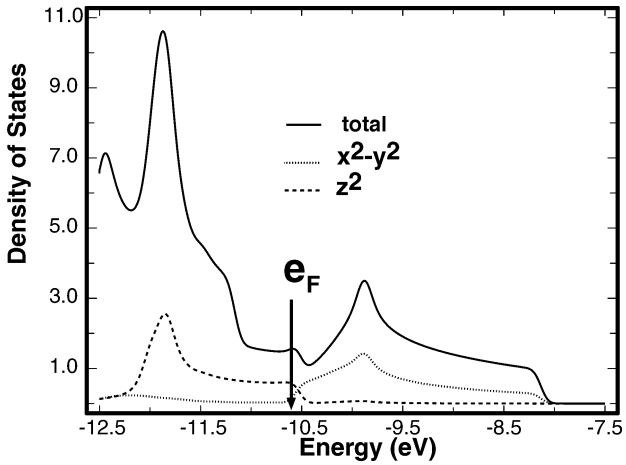

FIGURE 17.15
The density of states around the Fermi level, e_F, for $BaNiS_2$ at the extended Hückel level.

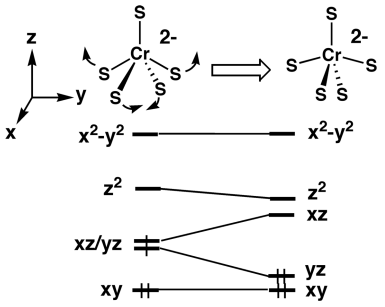

17.67

from that in $BaNiS_2$. One basal S–Cr–S opens up from 141.6° to 164.3° while the other angle narrows to 114.1°. In other words, the coordination geometry around Cr is very close to that of a trigonal bipyramid. Drawing from the Walsh diagram in Figure 17.4, **17.67** shows the correlation of orbitals going from the $BaNiS_2$ structure to the $BaCrS_2$ one. A gap is opened between the *xy*/*yz* set of orbitals and the *xz* states. As a result, $BaCrS_2$ is a semiconductor [68]. The structure of $BaCoS_2$ [69] is not much different from $BaNiS_2$. On the other hand an interesting structural variation is offered in $BaPdAs_2$ [70], **17.68**, with two less electrons. The basic

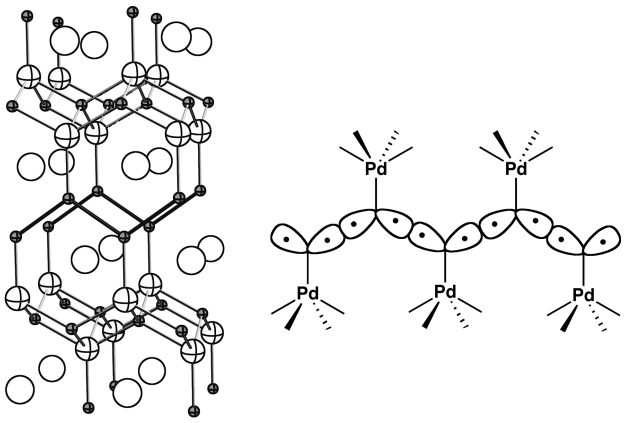

17.68 **17.69**

structure of $BaNiS_2$ is kept except that the registry of the layers with respect to each other is shifted so that As–As bonds are formed. The As–As bond length in these zigzag chains is 2.66 Å compared to 2.52 Å for elemental As. An easy way to view their formation starts with $BaNiS_2$. The apical S lone pairs for this compound are filled. Of the three lone pairs, let us take the a_1 combination (corresponding to the $2a_1$ in **17.62**) and one member of the *e* set (a *p* AO in the plane of what will become the As–As σ bonds) to form two hybrid orbitals at each apical As atom. In $BaPdAs_2$, consider that the two electrons removed come from these hybrids. After all, As is less electronegative than S, so these hybrids will lie at higher energy. As shown by **17.69**, the apical As–As σ bonds then are constructed from coupling the radical pairs. There are a number of compounds with one less electron; an example is $LnNiGe_2$ [71]. The situation here is not so clear cut; however, the majority of the electrons removed come from the π^* states associated with the apical Ge atoms (perpendicular to the plane in **17.69**).

PROBLEMS

17.1. a. Using $\chi_1 - \chi_5$ form SALCs at the square-pyramidal geometry shown below.

b. Interact the SALCS with the s, *p*, and *d* AOs of a transition metal. Draw the resultant orbitals.

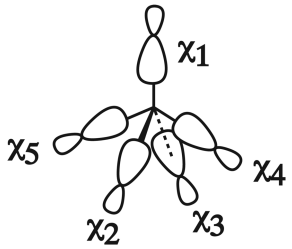

17.2. A d^8 square pyramidal $(CH_2)ML_4$ complex could have the carbene positioned in the apical or basal site. Determine which would be more favorable.

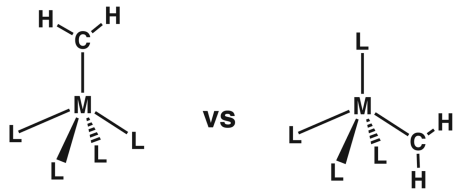

17.3. Pipes et al. [72] reported the preparation and structure of an unusual transition metal nitride. How many electrons are associated with the metal? What would be the level ordering and electron occupation for the Os *d* orbitals in this molecule?

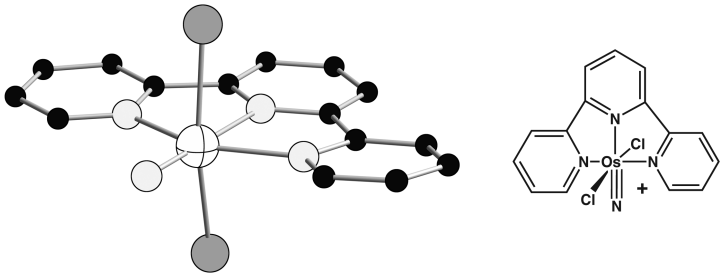

17.4. Acetylene complexes are fairly common; however, Nielson et al. [73] reported the structure of a d^4 tungsten complex, see below. Construct the important valence orbitals for this compound and indicate the orbital occupation.

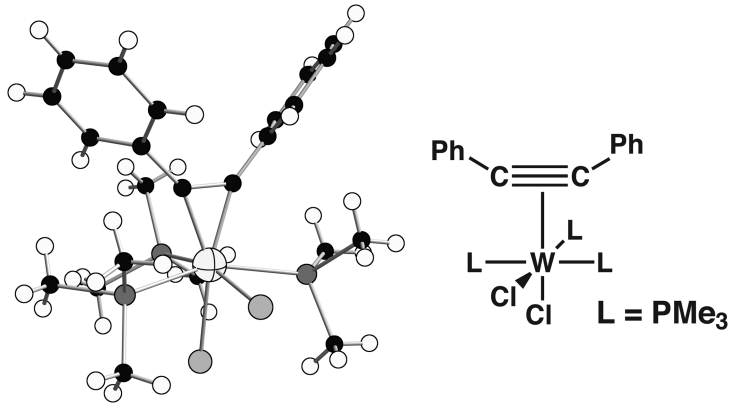

17.5. We introduced the bonding for dihydrogen complexes in Chapter 15. In general when the ligands L are good π-acceptors and/or the metal M exists in a high oxidation state, then these complexes can be observed. On the other hand, if these conditions are not met then transition metal dihydrides are found.

a. Describe why this occurs.

b. Sometimes one can initially observe dihydrogen complexes that then rearrange into dihydride products. What is the activation barrier that interconnects them?

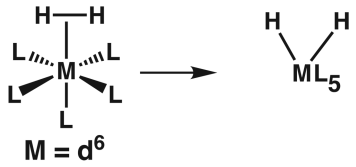

17.6. Section 17.5 discusses the bending in metal nitrosyl complexes. In this problem, we are going to go one step further with M–O_2 complexes. The heme adducts of O_2 involve a low spin Fe–porphyrin, a model of which is shown below (in actual fact this is a nitrosyl complex).

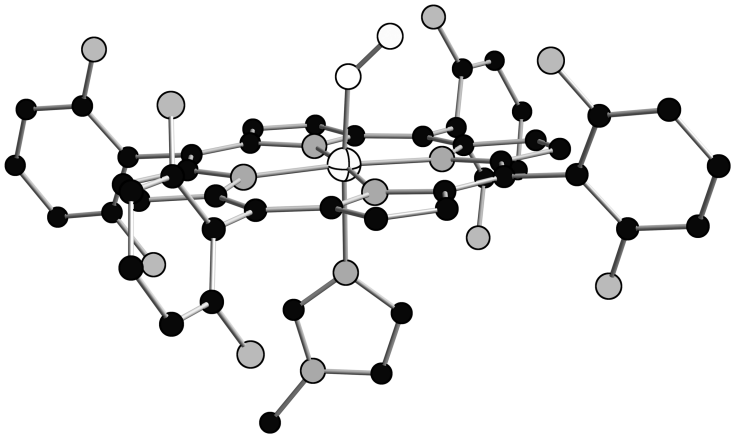

a. Using Figures 17.10 and 17.11 as models, determine whether or not the O_2 complex should be bent. When O_2 initially reacts, the iron porphyrin is high spin and, of course so is O_2. What should be the Fe—O—O bond angle in the initial adduct. You need to figure out what happens to $\pi^* - xz$ and $\pi^* - yz$, and add these curves

to Figure 17.11. Perhaps the easiest way to figure out what MOs are occupied is to count the O_2 ligand as being iso-electronic to CO or NO^+, that is, as O_2^{2+}.

b. If the M—O—O bending motion is continued, eventually the complex becomes an $(\eta^2\text{–}O_2)ML_4$ complex as shown below. Carefully work out the metal d, as well as, $\pi^* - xz$ and $\pi^* - yz$ MOs for the C_{4v} and C_{2v} geometries. Then, draw a Walsh diagram for the reaction path from C_{4v} to C_s to C_{2v}. What electron counts favor the $(\eta^2 - O_2)ML_4$ structure?

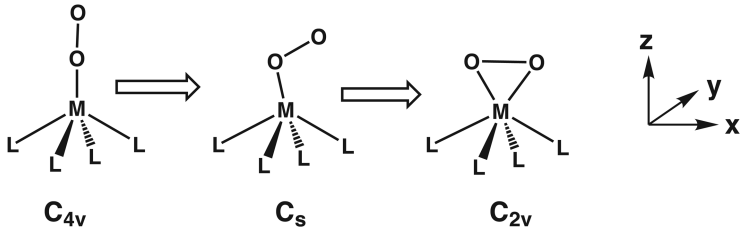

17.7. a. Determine the five SALCs for five generic ligands arranged in a pentagonal planar manner. Use these to interact with a transition metal's *s*, *d,* and *p* AOs.

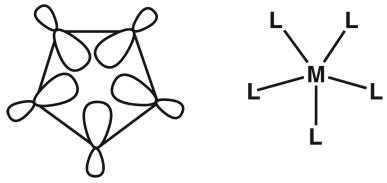

b. Form the MOs for a pentagonal bipyramid by interacting the orbitals in (a) with capping ligands. This is a common geometry for seven coordinate structures. An example provided below is from Reference 7 of Chapter 21. What other metal d^n electron counts should be stable at this geometry?

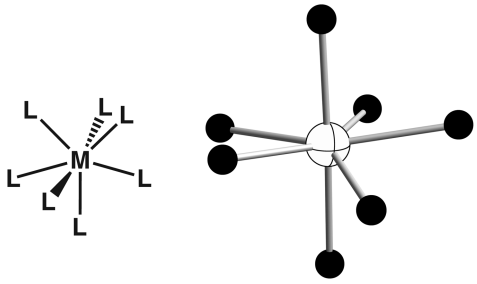

REFERENCES

1. M. Elian and R. Hoffmann, *Inorg. Chem.*, **14**, 1058 (1975).
2. R. Hoffmann, *Science*, **211**, 995 (1981).
3. T. A. Albright, *Tetrahedron*, **38**, 1339 (1982).
4. D. E. Sherwood and M. B. Hall, *Inorg. Chem.*, **22**, 93 (1983).
5. A. R. Rossi and R. Hoffmann, *Inorg. Chem.*, **14**, 365 (1975).
6. B. Roessler, S. Kleinhenz, and K. Seppelt, *Chem. Commun.*, 1039 (2000).
7. S. Groysman, I. Goldberg, M. Kol, and Z. Goldschmidt, *Oranometallics*, **22**, 3793 (2003).
8. C. J. Piersol, R. D. Profilet, P. E. Fanwick, and I. P. Rothwell, *Polyhedron*, **12**, 1779 (1993).
9. M. J. Paterson, P. A. Hunt, M. A. Robb, and O. Takahashi, *J. Phys. Chem. A*, **106**, 10494 (2002).

10. M. F. Perutz, H. Muirhead, J. M. Cox, and L. C. G. Goaman, *Nature*, **219**, 131 (1968).
11. A. J. Yencha, S. Canton, J. D. Bozek, and N. Berrh, *Report Number LBNL/ALS–43727*, July 1, 2001.
12. J. L. Hubbard and D. L. Lichtenberger, *J. Chem. Phys.*, **76**, 2660 (1981).
13. Y. Harada, K. Ohno, and H. Mutoh, *J. Chem. Phys.*, **79**, 3251 (1983).
14. C. Angeli, G. Berthier, C. Rolando, M. Sablier, C. Alcaraz, and O. Dutuit, *J. Chem. Phys.*, **101**, 7907 (1997); R. Fukuda, M. Ehara, H. Nakatsuji, N. Kishimoto, and K. Ohno, *J. Chem. Phys.*, **132**, 84302 (2010).
15. S. K. Kang, H. Tang, and T. A. Albright, *J. Am. Chem. Soc.*, **115**, 1971 (1993).
16. T. R. Ward, H.-B. Bürgi, F. Gilardoni, and J. Weber, *J. Am. Chem. Soc.*, **119**, 11974 (1997).
17. M. R. Cook, W. A. Herrmann, P. Kiprof, and J. Takacs, *J. Chem. Soc., Dalton Trans.*, 797 (1991).
18. J. K. Burdett, *Coord. Chem. Rev.*, **27**, 1 (1978).
19. Y. Ishikawa and K. Kawakami, *J. Chem. Phys., A*, **111**, 9940 (2007).
20. J. Kim, T. K. Kim, J. Kim, Y. S. Lee, and H. Ihee, *J. Chem. Phys., A*, **111**, 4697 (2007).
21. S, Alvarez and M. Llunell, *J. Chem. Soc., Dalton Trans.*, 3288 (2000).
22. S. A. Trushin, W. Fuß, and W. E. Schmid, *Chem. Phys.*, **259**, 313 (2000); S. A. Trushin, K. Kosma, W. Fuß, and W. E. Schmidt, *Chem. Phys.*, **347**, 309 (2008); For early work see M. Poliakoff and J. J. Turner, *Angew. Chem., Int. Ed.*, **40**, 2809 (2001); M. Poliakoff, *Inorg. Chem.*, **15**, 2022, 2892 (1976) and references therein.
23. G. Worth, G. Welch, and M. J. Paterson, *Mol. Phys.*, **104**, 1095 (2006).
24. A. Rosa, E. J. Baerends, S. J. A.van Gisbergen, E.van Lenthe, J. A. Groenveld, and J. G. Snijders, *J. Am. Chem. Soc.*, **121**, 10356 (1999) and references therein.
25. I. E. Rachidi, O. Eisenstein, and Y. Jean, *New J. Chem.*, **14**, 671 (1990).
26. G. R Clark, S. V. Hoskins, T. C. Jones, and W. R. Roper, *Chem. Commun.*, 719 (1983).
27. B. R. Bender, J. R. Norton, M. M. Miller, O. P. Anderson, and A. K. Rappe, *Organometallics*, **11**, 3427 (1992).
28. U. Radius, J. Sundermeyer, and H. Pritzkow, *Chem. Ber.*, **127**, 1827 (1994); U. Radius and R. Hoffmann, *Chem. Ber.*, **129**, 1345 (1996).
29. M. T. Youinou, J. Kress, J. Fischer, A. Aguero, and J. A. Osborn, *J. Am. Chem. Soc.*, **110**, 1488 (1988); See also, J. Kress, M. Wesolek, and J. A. Osborn, *J. Chem. Soc., Chem. Commun.*, 514 (1982).
30. J. R. Clark, P. E. Fanwick, and I, P. Rothwell, *Chem. Commun.*, 553 (1995).
31. A. Noll, S. Rabe, and U. Muller, *Z. Naturforsch.*, **54b**, 591 (1999).
32. P. Schwab, R. H. Grubbs, and J. W. Ziller, *J. Am. Chem. Soc.*, **118**, 100 (1996).
33. F. A. Cotton, C. A. Murillo, and R. A. Walton, editors. *Multiple Bonds Between Metal Atoms*, 3rd edition, Springer Science, New York (2005).
34. S. Shaik, R. Hoffmann, C. R. Fisel, and R. H. Summerville, *J. Am. Chem. Soc.*, **102**, 1194 (1980).
35. M. B. Hall, *J. Am. Chem. Soc.*, **97**, 2057 (1975).
36. Y. F. Hu, G. M. Bancroft, and K. H. Tan, *Inorg. Chem.*, **39**, 1255 (2000).
37. M. Grillone, F. Benetollo, G. Bombieri, and A.Del Pra, *J. Organomet. Chem.*, **575**, 193 (1999).
38. D. W. Hart, R. Bau, and T. F. Koetzle, *Organometallics* **4**, 1590 (1985).
39. P. Macchi, D. Donghi, and A. Sironi, *J. Am. Chem. Soc.*, **127**, 16494 (2005).
40. C. Mealli and L. Sacconi, *Inorg. Chem.*, **21**, 2870 (1982).
41. L. Q. Tang, M. S. Dadachov, and X. D. Zon, *Z. Kristallogr.*, **216**, 387 (2001).
42. Z. Mazej and E. Goresknik, *Eur. J. Inorg. Chem.*, 1795 (2008).
43. G. Ferey, J. Renaudin, Ade Kozak, and Y. Mary, *Eur. J. Solid State Chem.*, **26**, 427 (1989).
44. O. Horner, E. Anxolabehere-Mallart, M. F. Charlot, L. Tchertanov, J. Guilhern, T. A. Mattioli, A. Bossac, and J. J. Girerd, *Inorg. Chem.*, **38**, 1222 (1999).
45. H. Shorafa and K. Seppelt, *Z. Anorg. Allg. Chem.*, **635**, 112 (2009).

46. N. Matsumoto, M. Yamashita, I. Ueda, S. Kida, *Mem. Fac. Sci. Kyushu U., Ser. C* **11**, 209 (1978).
47. N. Matsushita, F. Fukuhara, and N. Kojima, *Acta Crystallogr.*, **E61**, i123 (2005) and references therein.
48. J. K. Burdett, *Inorg. Chem.*, **17**, 2537 (1978);J. K. Burdett, *J. Am. Chem. Soc.*, **101**, 5217 (1979).
49. M.-H. Whangbo and M. J. Foshee, *Inorg. Chem.*, **20**, 113 (1981).
50. L. V. Interrante, K. W. Browall, and F. P. Bundy, *Inorg. Chem.*, **13**, 1158 (1974).
51. B. A. Frenz, J. H. Enemark, and J. A. Ibers, *Inorg. Chem.*, **8**, 1288 (1969).
52. O. Alnaji, Y. Peres, M. Dartiguenave, F. Dahan, and Y. Dartiguenave, *Inorg. Chim. Acta*, **114**, 151 (1986).
53. R. B. English, M. M. de, V. Steyn, and R. J. Haines, *Polyhedron*, **6**, 1503 (1987).
54. R. Hoffmann, M. M-L Chen, M. Elian, A. R. Rossi, and D. M. P. Mingos, *Inorg. Chem.*, **13**, 2666 (1974).
55. J. H. Enemark and R. D. Feltham, *Coord. Chem. Rev.*, **13**, 339 (1974).
56. M. Chisholm, F. A. Cotton, and R. L. Kelly, *Inorg. Chem.*, **18**, 116 (1979).
57. B. Czeska, K. Dehnicke, and D. Fenske, *Z. Naturforsch.*, **B38**, 1031 (1983).
58. M. Pinsky and D. Avnir, *Inorg. Chem.*, **37**, 5575 (1998).
59. S. Alvarez and M. Liunell, *J. Chem. Soc., Dalton Trans.*, 3288 (2000).
60. R. Enjalbert and J. Galy, *Acta Crystallogr.*, **C42**, 1467 (1986).
61. S. Seong, K. A. Yee, and T. A. Albright, *J. Am. Chem. Soc.*, **115**, 1981 (1993).
62. J. G. Bednorz and K. A. Müller, *Angew. Chem. Int. Ed.*, **27**, 735 (1988).
63. M. K. Wu, J. R. Ashburn, C. J. Torng, P. H Hor, R. L. Meng, L. Goa, Z. J. Huang, Y. Q. Wang, and C. W. Chu, *Phys. Rev. Lett.* **58**, 908 (1987); P. H. Hor. L. Gao, R. L. Meng, Z. J Huang, Y. Q. Wang, K. Forster, J. Vassilious, C. W. Chu, M. K. Wu, J. R. Ashburn, and C. J. Torng, *Phys. Rev. Lett.* **58**[911] (1987).
64. M.-H. Whangbo, M. Evain, M. A. Beno, and J. M. Williams, *Inorg. Chem.* **26**, 1831 (1987); Inorg. Chem., **26**, 1832 (1987).
65. M.-H. Whangbo and C. C. Torardi, *Acc. Chem. Res.* **24**, **127** (1991) and references therein.
66. I. E. Grey and H. Steinfink, *J. Am. Chem. Soc.*, **92**, 5093 (1970).
67. L. F. Mattheiss, *Solid State Commun.*, **93**, 879 (1995); I. Hase, N. Shirakawa, and Y Nishihara, *J. Phys. Soc. Jpn.*, **64**, 2533 (1995).
68. O. Fuentes, C. Zheng, C. E. Check, J. Zhang, and G. Chancon, *Inorg. Chem.*, **38**, 1889 (1999).
69. M. C. Gelabert, N. E. Brese, F. J. DiSalvo, S. Jobic, P. Deniard, and R. Brec, *J. Solid State Chem.*, **127**, 211 (1996).
70. D. Johrendt, C. Lux, and A. Mewis, *Z. Naturforsch.*, **B51**, 1213 (1991).
71. D. M. Proserpio, G. Chacon, and C. Zheng, *Chem. Mater.*, **10**, 1286 (1998).
72. D. W. Pipes, M. Bakir, S. E. Vitols, D. J. Hodgson, and T. J. Meyer, *J. Am. Chem. Soc.*, **112**, 5507
73. A. J. Nielson, P. D. W. Boyd, G. R. Clark, P. A. Hunt, M. B. Hursthouse, J. B. Metson, C. E. F. Rickard, and P. A. Schwerdtfeger, *J. Chem. Soc., Dalton Trans.*, **112**, 11531995.